ACS OMEGA

http://pubs.acs.org/journal/acsodf

Review

Tissue Clearing and Its Application in the Musculoskeletal System

Yan-Jing Zhan, Shi-Wen Zhang, SongSong Zhu, and Nan Jiang*

Cite This: *ACS Omega* 2023, 8, 1739−1758

Read Online

ACCESS | Metrics & More | Article Recommendations

ABSTRACT: The musculoskeletal system is an integral part of the human body. Currently, most skeletal muscle research is conducted through conventional histological sections due to technological limitations and the structure of skeletal muscles. For studying and observing bones and muscles, there is an urgent need for three-dimensional, objective imaging technologies. Optical tissue-clearing technologies seem to offer a novel and accessible approach to research of the musculoskeletal system. Using this approach, the components which cause refraction or prevent light from penetrating into the tissue are physically and chemically eliminated; then the liquid in the tissue is replaced with high-refractive-index chemicals. This innovative method, which allows three-dimensional reconstruction at the cellular and subcellular scale, significantly improves imaging depth and resolution. Nonetheless, this technology was not originally developed to image bones or muscles. When compared with brain and nerve organs which have attracted considerable attention in this field, the musculoskeletal system contains fewer lipids and has high levels of hemoglobin, collagen fibers, and inorganic hydroxyapatite crystals. Currently, three-dimensional imaging methods are widely used in the diagnosis and treatment of skeletal and muscular illnesses. In this regard, it is vitally important to review and evaluate the optical tissue-clearing technologies currently employed in the musculoskeletal system, so that researchers may make an informed decision. In the meantime, this study offers guidelines and recommendations for expanding the use of this technology in the musculoskeletal system.

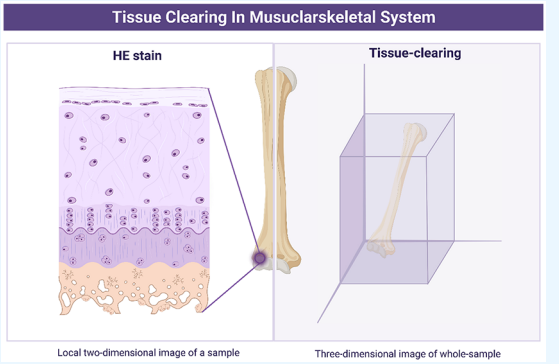

1. INTRODUCTION

1.1. Musculoskeletal System. Musculoskeletal tissue accounts for about a third of the total body weight. The health of the musculoskeletal system is indispensable for daily activities. According to the World Health Organization (WHO), about 1.71 billion people worldwide suffer from muscular−skeletal diseases.[1] In addition, due to the complex composition of the musculoskeletal system, such diseases are inclined to affect a variety of tissue structures with different functions. These structures include bones, muscles, ligaments, tendons, cartilage, etc. As the world population ages and risk factors (such as traffic accidents) increase, the number of people suffering from such diseases is expected to increase.[2] To slow the incidence of disorders, more research is needed on musculoskeletal tissues.

Classically, the musculoskeletal tissue is analyzed based on paraffin embedding or rozen section. Optical microscopy is an indispensable tool in the study of a musculoskeletal system. Currently widely used optical microscopes include two-photon excitation microscope, laser scanning confocal microscope, second harmonic microscope, etc. Despite being excellent for visualizing cells and pathways, these methods require sections of tissue.

1.2. Three-Dimensional (3D) Imaging. Through a micron-scale tissue section, conventional histology techniques can be used to study cell morphology or cell connections. Physiological changes and diseases do not exist only in selected embedded tissues. The full and comprehensive exploration of biological mechanisms in health and disease requires the manipulation of three-dimensional observations of the organism in situ.

For in situ 3D imaging, invasive and non-invasive imaging techniques are now available. The majority of invasive imaging is accomplished by imaging of continuous slices of samples and computer-assisted 3D reconstruction.[3,4] Nevertheless, this strategy has the following downsides: (1) it is time-consuming and arduous; (2) sample distortion is likely to occur; (3) the imaging cannot be repeated because samples have been destroyed;[5] and (4) the resolution on the *Z*-axis is limited to approximately 50 nm[4]. For non-invasive three-dimensional imaging of organisms, computed tomography (CT) and magnetic resonance imaging (MRI) are common. These techniques provide extensive, multiparameter information

Received: August 12, 2022
Accepted: December 7, 2022
Published: January 6, 2023

https://doi.org/10.1021/acsomega.2c05180
ACS Omega 2023, 8, 1739−1758

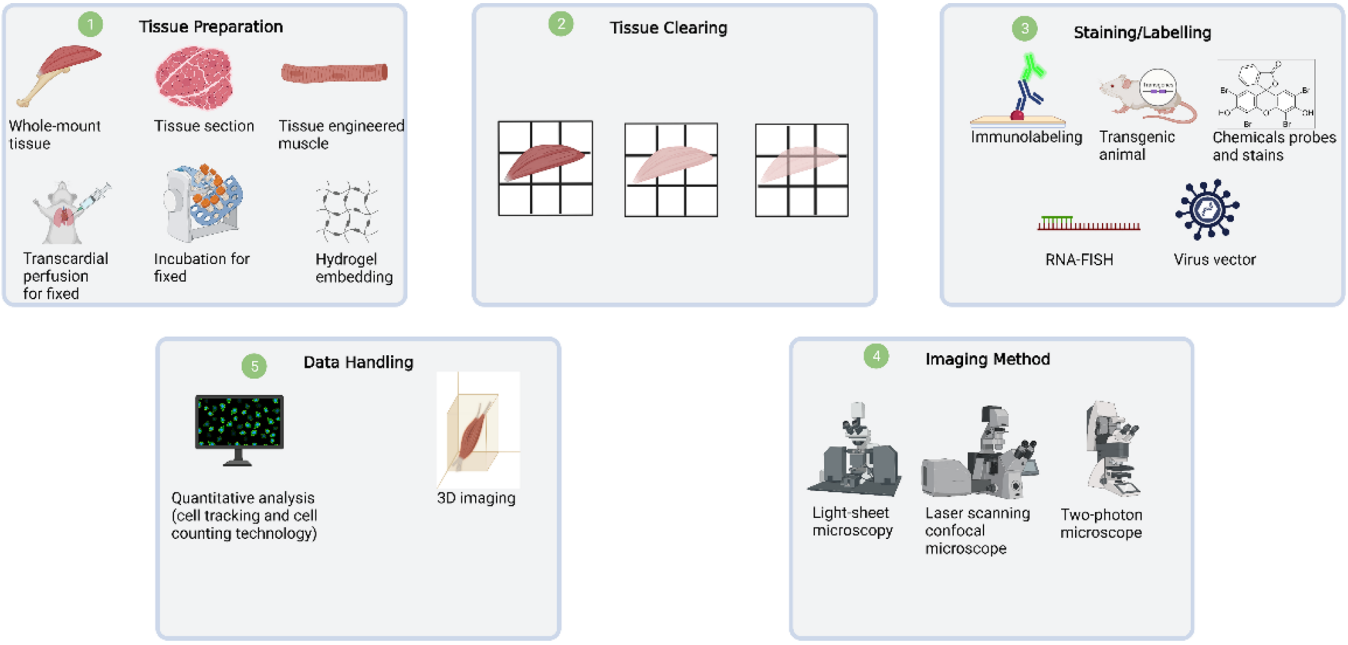

Figure 1. Steps for 3D imaging and analysis of the musculoskeletal tissues. (1) Tissue preparation. To perform 3D imaging and analysis, a target sample must first be obtained. This sample can be excised intact tissue (such as an extensor digitorum longus or femur), tissue sections of varying thickness, or tissue engineering samples. In addition, whole mice can also be cleared. There are three common methods for fixation of excised tissue: cardiac perfusion fixation, passive immersion fixation, and hydrogel embedding fixation. (2) Tissue-clearing. The samples can then be cleared with the appropriate OTCT following the fixation process. Most of the OTCTs are aimed at proteins, but a few are targeted at DNA and RNA. (3) Staining/labeling. Several techniques are available for labeling and staining targets, including immunostaining, chemical probes, transgenic mouse fluorescent protein, and fluorescence in situ hybridization (FISH). (4) Imaging method. Following this, the sample can be examined using light-sheet microscopy, confocal microscopy, and two-photon microscopy. (5) Data handling. The data obtained from imaging can be collected and stored by a computer for subsequent 3D reconstruction with the aim of analysis and extraction of information.

about humans, which can be useful for improving clinical diagnoses.[6] These methods, however, have poor resolution and cannot distinguish individual cells. In addition, any electrical noise at the MRI reception frequency will result in strip artifacts or an increase in picture noise.[6] Although the spatial resolution of nuclear magnetic resonance microscopy has risen to 100 μm,[7] it is still larger than the size of cells (e.g., cancer cell size of 10−25 μm[8]). Although two-photon excitation microscopy and confocal microscopy can achieve cellular resolution, their imaging depth is still insufficient for musculoskeletal system research. When these methods are used for whole-mount imaging, the resolution and contrast in deep tissue layers are negatively affected by light scattering. Bone tissue can only be imaged with confocal microscopy at 100−150 μm.[9] Similarly, cartilage can be imaged with a thickness of less than 100 μm[9]. Compared to confocal microscopy, the use of longer wavelength excitation light in two-photon microscopy increases the image depth but still limits it to 300 μm.[10,11] In recent years, optical tissue-clearing technology (OTCT) has improved imaging depth to several millimeters while maintaining a better resolution.

2. TISSUE-CLEARING TECHNIQUES

OTCT was proposed by Werner Spalteholz a century ago.[12] He combined methyl salicylate and benzyl benzoate to make animals transparent. This technology was not recognized until the invention and development of light-sheet fluorescence microscopy (LSFM) and computers, which overcame the obstacles in imaging, data storage, and data analysis. OTCT is becoming a promising tool for 3D imaging and has already been widely used in neuroscience, embryology, oncology, and other fields.[13,14] OTCT has improved the image depth to several millimeters or the whole-body sample. Tissues are composed of numerous constituents. According to subcellular level analysis, biological tissues consist of 70−80% water (refractive index (RI) 1.33), 10% proteins (RI 1.43), and 10% lipids (RI 1.44), among other components.[15] Hydroxyapatite (RI 1.60) is also present in the musculoskeletal system. Refraction of light occurs when light passes through a tissue with a non-uniform refractive index, which reduces the intensity of the light and makes tissues opaque. In addition to light refraction, light absorption also occurs during transmission, resulting in light attenuation.

The occurrence of light absorption in tissues is mainly attributed to a variety of pigment molecules in tissues, such as melanin, lipofuscin, and heme, which are widely present in the musculoskeletal system.[13] Although light absorption has less of an impact than refraction, decolorization often occurs during the clearing procedure to achieve a more effective clearing result. A simple explanation of the OTCT process is that light absorption is reduced and the tissue's refractive index (RI) is balanced. OTCT generally starts with the removal of endogenous pigments, substances with a relatively low RI (water and/or lipids), and substances with a relatively high RI (hydroxyl apatite). Next, a reagent with a particular RI is used to infiltrate the treated tissue. As a result, the RI of the sample and that of the reagent tend to be consistent, resulting in transparency. There are additional OTCTs listed below that do not apply delipidation and dehydration but instead use hyperhydration to obtain a sample RI near to that of water. For a deeper understanding of the physicochemical principles

https://doi.org/10.1021/acsomega.2c05180
ACS Omega 2023, 8, 1739−1758

of tissue-clearing, we recommend reading the cited references.[16−19]

2.1. Superiority of OTCT in the Musculoskeletal System. Musculoskeletal cells are interconnected in three dimensions to form a complex structure. In musculoskeletal diseases, changes in tissue and structure can be limited to tissue surfaces or paraffin-embedded tissues without OTCT.

In terms of composition, bone is composed of 50% to 70% inorganic or mineral content, 20% to 40% organic matrix, 5% to 10% water, and <3% lipids.[20] The bone organic matrix contains collagens (90%), mainly type I collagens and some noncollagenous proteins, such as osteocalcin.[21] Hyaline cartilage (such as articular cartilage) and fibrocartilage (such as articular cartilage discs) are closely linked to the musculoskeletal system. Hyaloid cartilage contains collagenous fibrils composed of type II collagen, which are interwoven and form a dense extracellular matrix network together with extracellular chondromucin. Fibrocartilage is mainly composed of type I collagen with a relatively low proteoglycan aggregate content.[22] Chondrocytes are arranged in bands and embedded in a dense network for collagen fibrils and proteoglycans.[23] From the above description, the complex composition results in significant light scattering, limiting the imaging depth of the skeleton. Even with the use of confocal microscopy and other advanced optical microscopy techniques, the musculoskeletal system is rich in collagen fibers, proteoglcans, and minerals, which limit the absorption of excitation energy and increase the scattering of excited and emitted fluorescent photons.[24]

The structure of the musculoskeletal system has an obvious hierarchy. Compared with ectochondral cells, deep layers have heterogeneous phenotypes and morphologies. On the surface of joints, chondrocytes are flat, and the type II collagen fibers are interwoven and arranged parallel to the surface.[22] The cells gradually become spherical but are less abundant in the middle layer just beneath the articular cartilage, and type II collagen is widely dispersed. The number of cells in deep tissue is reduced even further, but the fiber diameter is expanded. Specific hypertrophic chondrocytes secrete TypeX collagen in the transition area between deep cartilage and subchondral bone. Type II collagen fibers are oriented perpendicular to calcified cartilage and subchondral bone in the deep layer.[22] As a result, the majority of tissues in the musculoskeletal system have structural variability at different levels. Traditional histological procedures can result in the loss of much in situ cell information due to mechanical dissection of the tissue.

Deep tissue abnormalities have been seen in numerous musculoskeletal illnesses, according to recent research. Degenerative alterations resulting from osteoarthritis, for example, occur in the deep layer, with stratification of calcified cartilage and bone, as well as the enlargement and replacement of surface articular cartilage by calcified cartilage area.[25] The pericellular matrix (PCM), a small stromal area surrounding chondrocytes, is directly linked to osteoarthritis formatting at the cellular level. On the other hand, the PCM is only 2−4 μm thick.[26] As a result, the lack of in situ 3D imaging of skeletal muscle tissue structure or even cells will restrict further research of skeletal muscle disorders and their treatments (Figure 1).

2.2. General Steps for OTCT. In general, OTCTs involve fixation, delipidation, decolorization, dehydration, RI matching, and imaging. In a broader sense, the permeabilization process encompasses steps such as delipidation, dehydration, and hyperhydration, all of which promote further permeation of exogenous molecules. In a narrow sense, permeabilization mainly refers to the addition of additional osmotic promoting agents. For example, Jin et al. found that thiazolone effectively promotes the transfer of clearance agents through the skin, which is effective in permeabilizing the skin but is not relevant to muscle tissues.[27]

Depending on the research purpose, different clearing methods involve different arrangements and combinations of the main steps. Some specific steps are also added to achieve the optimal effect in a specific tissue. As a result, various OTCTs have distinct benefits and limitations, as well as optimal tissues for application. The musculoskeletal system has a unique composition, consisting of high-RI hydroxyapatite and light-absorbing heme in muscles and bones. The decalcification steps and decolorization are particularly critical in achieving an excellent musculoskeletal system clearing effect.

2.2.1. Perfusion and Fixation. Since early OTCTs do not include heart perfusion, clearing blood-rich tissues is challenging (such as the spleen, kidney, and muscles). When compared to immersion in a decolorization solution, cardiac perfusion can effectively and universally remove blood from tissues, increasing the transparency of biological specimens. Most OTCTs now start with cardiac perfusion, specifically when used for whole-body imaging. For example, in PEGASOS, phosphate-buffered saline (PBS) or saline is administered into the left ventricle of mice shortly after general anesthesia to substitute the blood.

The completion of effective perfusion is indicated when the blood-rich organs turn white (for example, when the color of the liver and spleen changes from red to white).[28] Of course, passive immersion can be used to achieve optimal results without cardiac perfusion for biological samples with smaller volumes and little coloring (tissues lacking hemoglobin, melanin, and so on).

Currently, the majority of studies focus on imaging proteins in biological samples, with only a few studies focusing on imaging tiny molecules, such as DNA and dopamine.[29,30] As a consequence, different physical and chemical properties of reagents should be chosen for the fixation of samples depending on the research object. Paraformaldehyde (PFA) is currently the most commonly used fixation reagent, but it can only fix the physically continuous protein network and cannot chemically fix free proteins.[18]

Fixation with hydrogel embedding may be an alternative for imaging free proteins in tissue. Free proteins can be trapped in the gel because hydrogels are covalently bonded to proteins via the acrylamide gel matrix.[18] The glutaraldehyde fixation technique can be used to improve the protective ability of fluorescent proteins and antigen epitopes. The protein preservation ability of SWITCH-based glutaraldehyde reagent is marvelous. Fixed samples even enable high-temperature boiling delipidation treatment (80 °C).[30] However, the high reactivity of glutaraldehyde with tissue causes it to rapidly react with the outer layers of the tissue and to rapidly become depleted. To fixed large specimens with glutaraldehyde, pH adjustments must be applied to regulate the reaction speed and fixation effect.

2.2.2. Hydrogel Embedding (for Hydrogel Embedding-Based Clearing Methods). Using CLARITY-based techniques, tissue must be hydrogel-embedded. As mentioned in Section 2.3, this method efficiently preserves the free proteins in tissues. However, the hydrogel cross-linked structure maintains lipid molecules, which makes adequate clearance impossible

https://doi.org/10.1021/acsomega.2c05180
ACS Omega 2023, 8, 1739−1758

without effective delipidation. The major components of the hydrogel solution are acrylamide, bis(acrylamide), and 2,2′-azobis[2-(2-imidazolin-2-yl)propane]dihydrochloride (VA-044).[29] Cardiac perfusion or tissue-embedding can be used to embed hydrogels. To avoid compromising hydrogel formation, oxygen should be removed from the centrifuge tube and the embedded tissue sample. In the presence of SDS and electrophoretic delipidation, tissue volume can increase but can be returned to normal after application of a clearing reagent.[29]

2.2.3. Decalcification (for Bone and Bones). The RI of hydroxyapatite in bone is the highest in the body, which might result in an obvious reflection of light during transmission.[15] As a result, decalcification is required to further equalize the RI of the samples. In the early stages of OTCT development, inorganic acids such as nitrate and hydrochloric acid were used to remove calcium. These acids function well but degrade osseous tissues.[19] Due to a lack of technical assistance, early OTCTs did not necessitate fluorescence imaging; hence, such reagents were frequently utilized in the early phases.

The most commonly used decalcification reagent is ethylene diamine tetraacetic acid (EDTA). The action of EDTA is based on the collection of calcium ions from the surface of hydroxyapatite. Moderate decalcification with EDTA can protect antigen activity and fluorescence signals.[15] EDTA causes minimal tissue damage and can even be utilized in vivo to study structures such as the cerebral cortex and blood arteries via OTCT.[31] During a screening of CUBIC-related decalcification regents, Tainaka and colleagues discovered that a mixture of EDTA and imidazole might achieve enhanced clearing efficiency.[32] Mouse bones were decalcified using the PEGASOS procedure, which involved application of a 20% EDTA solution (pH 7.0) for 4 days. Increases in sample size require longer decalcification times. Passive CLARITY (PACT) in combination with EDTA (pH 8.0) can also be used to clear bone tissue (PACT-deCAL).[32]

2.2.4. Decolorization/Pigment. A variety of pigments can be found in biological samples, including hemochrome, melanin, lipofuscin, riboflavin, and others. In addition to being one of the most abundant pigments in the human body, hemoglobin is most abundant in muscles and bone marrow.

These endogenous pigments have a substantial impact on light penetration. Even when cardiac perfusion is used to restore blood in tissue, blood remains in most blood-rich organs. iDISCO employs the powerful oxidant hydrogen peroxide (H_2O_2) for pigment bleaching, which can achieve quick bleaching of practically all pigments, including hemoglobin, melanin, lipofuscin, and riboflavin. However, unexpected protein degradation occurs as a result of its powerful and nonselective bleaching, including loss of endogenous fluorescent signal and antigenicity.[18] As a result, in iDISCO, endogenous fluorescent proteins should always be relabeled.

Amino alcohols, such as *N*-butyldiethanolamine or Quadrol can successfully decolorize hemoglobin.[33] This may be because the basic nitrogen in amino alcohols outcompetes the histidine in globin for binding to the iron-containing heme.[18,32,33] Furthermore, CLARITY can achieve effective decolorization of hemoglobin, the mechanism of which is unknown but may be connected to electrophoresis and/or sodium dodecyl sulfate (SDS) denaturation of the heme holoenzyme.[18,34] However, these approaches are insufficient for removing large volumes of pigments like melanin, which may explain why many OTCTs fail to clear the pigment in the epithelium.[28,35]

OTCTs based on fructose[36,37] and glutaraldehyde[30] have been shown to cause Maillard reactions, resulting in browning of the sample and enhanced self-fluorescence.[19] On the other hand, glycerin and sodium sulfite can assist in decreasing the color change induced by this reaction.

2.2.5. Dehydration (for Hydrophilic Tissue-Clearing Method). Dehydration is a common step in hydrophobic tissue-clearing techniques. Since high-refractive-index cleaning agents are immiscible with water, dehydration and delipidation are often performed concurrently. Dehydration facilitates the penetration of high-RI reagents. The early clearing procedures used graded ethanol for dehydration, but the tissue became rigid and the dehydration impact was weak, causing significant quenching of fluorescent proteins. Therefore, ethanol has been substituted by tetrahydrofuran (THF) with green fluorescent protein (GFP) protection.[38] Additionally, other alcohols, such as 1-propanol,[39] tert-butanol,[28,40] and methanol,[41] have few detrimental effects on fluorescence signals and tissue shape and can also be utilized for dehydration. Since water is essential for the preservation of fluorescence signal, even minor dehydration reagents may harm fluorescent proteins. Several hydrophobic technologies have been developed to protect fluorescent molecules, including PEGASOS, which uses modified polyethylene glycol (PEG) to create a favorable environment for GFP molecules.[28]

2.2.6. Delipidation/Lipid Removal. Delipidation is used in most OTCTs to increase the permeability of tissues. The reason for this is that lipids have a high RI, and the presence of a lipid bilayer inhibits the infiltration of macromolecule RI matching reagents. Current approaches to increasing permeability through delipidation include hydrophobic, hydrogel-based, and partial hyperhydration tissue-clearing methods.

In the early stage of development of hydrophobic methods, ethanol was selected for dehydration and delipidation, but the delipidation effect was not sufficient to clear lipid-rich tissues. Subsequently, THF and dichloromethane (DCM) were gradually screened out for delipidation.[42] Despite the poor delipidation effect of ethanol, 1-propylene glycol and *tert*-butanol are excellent delipidators.[28,40] TDE, as screened by Nemoto's and Pavone's teams, is also capable of delipidation, but cannot fully clear adult mouse brains.

SDS, a highly fat-soluble ionic detergent, is used for delipidation in CLARITY-based hydrogel-embedded tissue-clearing technologies. However, the clearing efficiency of SDS applied via passive immersion is mediocre, which may be related to the molecular volume. Adding urea,[43] creating an electric field,[34,44] cardiac perfusion,[33,45] and heating[30] can improve SDS delipidation efficiency. Heating is not applicable to PFA-fixed samples, but does apply to the SWITCH-based glutaraldehyde-fixed samples indicated above. Urea is an osmotic small molecule that can pass quickly through the lipid bilayer to raise intracellular osmotic pressure and improve the transit of other reagents.[46]

Detergents and amino alcohols are crucial for the degradation steps in hyperhydration techniques. Triton X-100 is a commonly used detergent that works by coating lipid particles. Partial OTCTs can also benefit from saponins.[47] Among amino alcohols, Quadrol and triethanolamine have significant delipidation capability. Ueda's team developed Sca*l*e CUBIC-1, a cocktail reagent consisting of urea, Quadrol, and

https://doi.org/10.1021/acsomega.2c05180
ACS Omega 2023, 8, 1739−1758

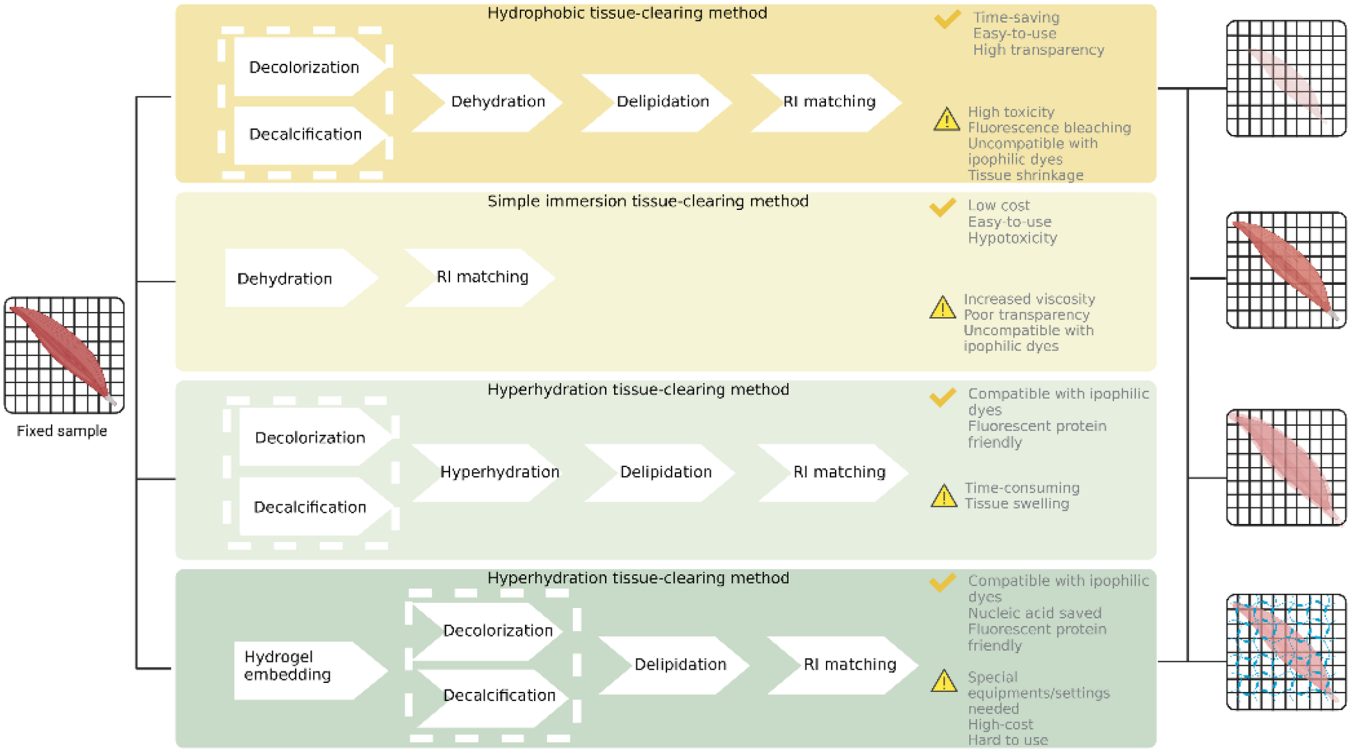

Figure 2. Different steps for the four classifications of tissue-clearing techniques. The hydrophobic tissue-clearing method is mainly composed of dehydration, delipidation, and RI matching. Hydrophilic tissue-clearing methods in this study include simple immersion tissue-clearing, hyperhydration tissue-clearing, and hydrogel-based tissue-clearing. For simple immersion, dehydration is achieved through the immersion of tissues and accompanied by RI matching. Hyperhydration tissue-clearing methods involve hyperhydration, delipidation, and RI matching. As for hydrogel-based tissue-clearing methods, samples need to be hydrogel-embedded and then followed by delipidation and RI matching.

Triton X-100 which can be used in conjunction with Sca*l*e CUBIC-2 to achieve efficient delipidation results.[48]

2.2.7. Hyperhydration. Urea and fructose are currently the most often used hyperhydration agents. Urea has a high hydration capacity and can swiftly move through the cell membrane without being hampered by the lipid bilayer. Additionally, its penetration-enhancing effect may enhance the further infiltration of clearing reagent into samples, resulting in better clearing effect than the simple immersion method.[18] Urea-treated tissue is also compatible with lipophilic chemicals and dyes compared with hydrophobic methods. However, the weak denaturation of proteins induced by urea on protein may cause tissue swelling.

Although fructose is a frequent hyperhydration agent,[37] fructose-treated samples are prone to the Maillard reaction, and the viscosity increases dramatically, compromising sample operation and storage and resulting in the introduction of difficult-to-remove bubbles.

2.2.8. RI Matching. One of the basic mechanisms of OTCTs is RI matching. Contrast agents (such as iodohyl[45]), polyols (glycerol, sorbitol,[45] fructose,[49] and others), and amide compounds are currently used as clearing reagents. Traditionally, the clearing reagents employed in OTCTs are frequently a blend of high-RI reagents. As protein in tissues is frequently treated as a research target, RI matching is frequently accomplished by removing lower RI intracellular and extracellular fluid, along with higher RI lipids. Generally, if the study goal is altered, the RI matching target value can be adjusted as well.

2.3. Classification of Optical Tissue-Clearing Techniques. OTCTs can generally be categorized according to the properties of the reagents utilized in clearing and the change in RI after clearing. At present, a detailed and unified classification has not been proposed. Scholars have put forward a variety of classifications according to different standards and intentions, among which there are two widely accepted classifications. The first classification divides OTCTs into the following: hydrophobic tissue-clearing method (also known as solvent tissue-clearing method), hydrophilic tissue-clearing methods (also called aqueous tissue-clearing methods) ,and hydrogel-based tissue-clearing methods.[14] Another type of classification incorporates hydrogel-based tissue-clearing methods into hydrophilic tissue-clearing methods; thus it only includes hydrophobic tissue-clearing methods and hydrophilic tissue-clearing methods. Additionally, hydrophilic tissue-clearing methods were further classified based on the differences among them. Consequently, the hydrophilic tissue-clearing method is further divided into the following three categories: simple immersion, hyperhydration, and hydrogel-based methods.[50] For an explanation of the first classification, we suggest further reading of the recommended reference.[14]

2.3.1. Hydrophobic Tissue-Clearing Method. The main difference between the hydrophobic tissue-clearing method and other methods is that the hydrophobic method utilizes organic solvents, which remove most of the lipids from the tissues during dehydration. In using this method, it is possible to obtain a dehydrated, delipidized, protein-rich, dense, and contracted sample. After dehydration, the main component of the sample is protein, and thus the RI is higher than 1.5.[50] Therefore, the RI of the clearing agents must be above 1.5 to penetrate into the sample and match the RI of the sample.

https://doi.org/10.1021/acsomega.2c05180
ACS Omega 2023, 8, 1739−1758

Additionally, in this method, the selected clearing agents must have the ability to dissolve the residual lipids in the delipidated tissue. Light scattering in tissues is primarily caused by lipids and hydrophobic clearing reagents have a higher RI (1.43∼1.47) than reagents used in other techniques,[51] resulting in a significant clearing effect in a relatively short amount of time with the hydrophobic method. Through the hydrophobic clearing method, water is removed from the sample, which is essential for maintaining the proteins fluorophores. As a consequence, this method has a pronounced negative effect on protein fluorescence compared with the hydrophilic tissue-clearing method. In addition, this method cannot be used with lipophilic dyes (e.g., DiI).

The common hydrophobic tissue-clearing method including benzyl alcohol and benzyl benzoate (BABB),[52] 3DISCO (three-dimensional imaging of solvent-cleared organs),[38] ultimate DISCO (uDISCO),[40] immunolabeling-enabled DISCO (iDISCO),[53] iDISCO+,[41] FluoClearBABB,[39] ethyl cinnamate (ECi),[54] free-of-acrylamide SDS-based tissue-clearing (FASTClear),[55] polyethylene glycol (PEG)-associated solvent system (PEGASOS),[28] variable domain of heavy chain antibodies (nanobodies) DISCO (vDISCO),[56] DISCO with superior fluorescence-preserving capability (FDISCO),[57] and stabilized DISCO (sDISCO).[58]

Hydrophobic methods are generally capable of efficiently clearing samples, result in high sample strength, and require little sample preparation time. However, their extensive use is limited due to a number of hazards including the high toxicity of organic reagents, incompatibility with membrane-labeled dyes, distinct shrinkage of samples, and quenching of fluorescent proteins.[59] In addition, the clearing reagents may dissolve the glue used to construct the objective during the imaging procedure[50] (Figure 2).

2.3.2. Simple Immersion Tissue-Clearing Method. Simple immersion tissue-clearing is a traditional hydrophilic tissue-clearing methods which mainly based on the clearing effect of fructose and urea. The difference between this technology and other hydrophilic methods is that its transparency is achieved by immersing the sample in a high-RI solvent (RI 1.37∼1.52). Considering the high viscosity of fructose, this method will cause bubbles in clearing system. FRUIT method mingled urea and fructose to reduce viscosity while TDE addressed this issue through diluting with water.

Furthermore, simple immersion methods overcome the limitations of hydrophobic methods in preserving lipids. Since the clearing effect fluctuates with the penetration efficiency of clearing reagents, this method is more reliable for the clearing of small-volume samples, but it is not suitable for larger samples.

The common simple immersion tissue-clearing method including Sucrose,[60] FocusClear, 2,2′-thiodiethanol (TDE),[61] a cocktail of fructose and urea (FRUIT),[37] See Deep Brain (SeeDB),[36] Clear^{T}/Clear^{T2},[62] etc.

Generally, only small-volume samples are eligible for these protocols. Since the lipids are retained, the clearing effect is not as ideal as that in hydrophobic methods and other hydrophilic methods. However, this method has the advantages of simplicity, low cost, and compatibility with a wide range of fluorescent dyes and proteins (including lipophilic dyes) (Figure 2).

2.3.3. Hyperhydration Tissue-Clearing Method. Considering that high-refractive-index molecules are bulky and have difficulty diffusing into tissue and that lipid bilayers determine the permeability of cells, delipidation is the key step in improving tissue permeability and transparency. Compared with lipid retention methods, hyperhydration clearing technologies use detergent-based (such as Triton X-100) lipid removal methods combined with nonhydrophobic solvents to clear the remaining tissue. The clearing reagents used in this technology are mostly based on urea. Common hyperhydration clearing methods include: Scale,[43] Clear, unobstructed brain imaging cocktails and computational analysis (CUBIC),[49] mxylylenediamine-based aqueous clearing system (MACS),[63] ScaleS,[64] SeeDB2[65] and clearing-enhanced 3D microscopy (Ce3D),[65] etc. Upon penetration of urea into the hydrophobic region of a high-refractive-index protein, the protein can be partially denatured and hydrated, and this overhydration status reduces the RI to 1.38.[50] With this method, the sample volume can be significantly increased, which is likely related to the partial denaturation proteins.

In conclusion, the distinction between hyperhydration and simple immersion techniques resides in the elimination of lipids and the lowering of the RI. As a result, the hyperhydration technique has a greater clearing impact than simple immersion. However, it is easy to induce sample expansion. In studies that require a fine-grained observation of the relative location of internal structures, this approach should be used with caution, or an alternative clearing method can be employed instead (Figure 2).

2.3.4. Hydrogel Embedding-Based Clearing Method. Common hydrogel embedding-based clearing methods including clear lipid-exchanged acrylamide-hybridized rigid imaging/immunostaining/in situ hybridization-compatible tissue-hydrogel (CLARITY),[34] Stabilization to harsh conditions via intramolecular epoxide linkages to prevent degradation (SHIELD),[44] perfusion-assisted agent release in situ (PARS),[66] simplified CLARITY method (SCM),[67] passive clarity technique (PACT),[66] and system-wide control of interaction time and kinetics of chemicals (SWITCH).[30]

For RI matching, this approach employs intermediate RI (1.45−1.50) clearing agents.[68] Lipids can be successfully removed with detergents. The impact of detergents is the basis of all CLARITY-related clearing technologies. Hydrogel embedding gives tissues a physical framework and creates covalent bonds with biomolecules, including proteins and nucleic acids, effectively preserving molecular information. In CLARITY, samples can be delipidated via electrophoresis-driven or passive clearing, resulting in dramatically enhanced permeability and transparency. However, staining of larger tissues demands longer incubation times. Currently, there are two methods for increasing the effectiveness of molecular probe penetration (antibodies). The first is to reduce gel density and cross-linking to enhance the permeability of molecular probes, but this weakens the capacity of the hydrogel to protect cellular structure and molecular information. The use of stochastic electrotransport, powered by an electric field, to enable the accelerated diffusion of molecules (e.g., antibodies, dyes, and detergents) into dense tissue−gel complexes,[14] is another approach used in techniques such as PACT.

In conclusion, hydrogel embedding-based clearing methods can minimize the structural damage to samples and protect the biomolecular information to the greatest extent while ensuring effective delipidation by detergents. These techniques facilitate the localization and study of biomolecules at subcellular resolution in whole-body-scale cleared samples (Figure 2).

https://doi.org/10.1021/acsomega.2c05180
ACS Omega 2023, 8, 1739−1758

3. MUSCLES

3.1. Skeletal Muscle Blood Vessels and Nerves. The modified BABB method was employed by Dickie's team to achieve whole-mount clearing in adult mice. Endothelial cells were stained with lectin through cardiac infusion. To extend the labeling period, the microvascular system was then filled with fluorescent nanoparticles.[69] Other labeling approaches, such as nuclear labeling, are compatible with this vascular labeling strategy. After BABB treatment, there was no visible photobleaching. The microvessel imaging depth in muscle and cardiac tissue can be enhanced to 1500 μm using this technology.[69] Based on the findings of Milgroom et al.,[70] Feng's group investigated the use of passive CLARITY to image skeletal muscles and was able to produce specific staining of vessels, neurons, and nuclei and to increase the imaging depth to 250 μm.[71] Feng's group was able to overcome Milgroom's inability to label actin and the neuromuscular junction (NMJ) while also increasing imaging depth.[70,71] However, it should be emphasized that labeling the quadriceps femoris in cleared mice requires approximately 40 days.

3.2. Neuromuscular Junction (Motor End Plates). Milgroom et al. demonstrated that CLARITY can be utilized to clear skeletal muscle in the mouse hindlimb. The position of the Hoechst 33342-stained muscle cell nuclei did not vary significantly when the autofluorescence results of the experimental and control groups were assessed, suggesting that CLARITY can clear mouse skeletal muscle without altering muscle structure.[70] However, the application of CLARITY was not suitable for tendons, as reported by Calve. Milgroom suggests that the lack of adipose tissue in the tendon is responsible. Milgroom's group has attempted several times to visualize neuromuscular connections by using fluorescently labeled cyclotoxin, but even the most superficial muscle fibers could not be successfully labeled. In addition, fluorescently labeled phalloidin was unable to efficiently identify actin.[70] The most extensively utilized marker of the postsynaptic NMJ is cyclotoxin. If CLARITY cannot be used to image neuromuscular connections, it will become an inherent flaw in muscle tissue research. Williams verified Milgroom's findings that CLARITY is incompatible with cyclotoxin. They hypothesized that the SDS employed in CLARITY might quench fluorescence or denaturate acetylcholine receptors (AChRs).[72] To obtain NMJ immunolabeling in skeletal muscle, Williams' group proposed the MYOCLEAR protocol based on CLARITY. Since SDS was not utilized to delipidate the samples, this approach was able to clear and stain NMJs in samples with a thickness of more than 700 μm. This technique not only allowed successful imaging of the healthy extensor digitorum longus and diaphragm but also imaging of the highly fibrotic muscle tissue of dystrophic mice.[72] According to Williams' research,[72] MYOCLEAR is capable of protecting the normal anatomy of the NMJ (containing presynaptic tissue, postsynaptic tissue, and synaptic cleft).[72]

Yin's team has performed experiments with OTCT, the majority of which focus on 3D imaging and the impact of disease on NMJs. By analyzing the clearing effects of various OTCTs, they chose the 3DISCO[73] method compared to Williams' study group. The 3DISCO method was also found to be compatible with α-cyclotoxin labeling of motor end plates. They discovered that injecting cyclotoxin intravenously is an effective and time-saving labeling approach.[74] In isolated mouse muscle, NMJs can be clearly seen after 1 h of treatment with a 0.3 g/g dose of cyclotoxin.[74] They cleared numerous muscles in mice (including the quadriceps, triceps, and biceps) and identified motor end plates and their 3D distribution in intact (undissected) muscles. The findings revealed that motor end plates were dispersed in lamella clusters, with each muscle having its own specific lamella clusters. The lamellar clusters of the gastrocnemius muscle in normal mice have an "M" form, and the lamellar cluster can recover to this shape after reinnervation in denervated mice.[73] According to them, muscles in traditional anatomy can be classified into additional functional units by further subdividing the distribution of lamella clusters. This will provide a structural basis for more precise electrophysiological examinations and intramuscular drug delivery.[73]

Zhu's team employed FDISCO (DISCO with superior fluorescence-preserving capability) to replicate Yin's findings: after clearing the gastrocnemius and tibialis anterior muscles, they discovered that the motor end plate is distributed in distinct lamella clusters in various muscles. Based on the 3D distribution of the motor end plate, they carried out 3D intramuscular injections with much higher efficiency than two-dimensional injections. The effectiveness of retrograde transport can also be enhanced according to the 3D distribution of the motor end plate.[75] The efficacy of 3D injected muscle labeling improved gradually as skeletal muscle volume increased. In the clinic, this will enhance the therapeutic effect on muscles and peripheral motor nerves. They subsequently examined the alterations in the motor end plates of mice after peripheral nerve damage using a combination of these approaches. They discovered that mice with delayed peripheral nerve regeneration exhibited an irregular gastrocnemius NMJ morphology, a less uniform fluorescence signal, a smaller mean area, and decreased maturity.[76]

3.3. Skeletal Muscle Tissue and Bioartificial Muscle. In visible spectrum imaging, skeletal muscle tissue has strong autofluorescence, hindering the imaging of target fluorescence. By combining numerous second-harmonic-sensitive proteins with a selected TDE-based clearing technology, Friedrich's group successfully performed label-free imaging of cardiotoxin (CTX)-induced muscle necrosis in mice.[77] The imaging data replicated the necrotic characteristics seen in HE slices. Second harmonic imaging showed that the myosin-II signal in the necrotic area was entirely lost, while the fibrocollagen signal intensity remained constant.[77] This approach provides more detailed information and more precise delineation of necrotic muscle tissue than HE slices and thus has promising applications in the musculoskeletal system.

Additionally, OTCTs may be employed to analyze diseased muscles. For the first time, Bozycki's group employed CUBIC to quantify whole-body calcium deposition in mdx mice. Calcified deposits were seen in the forelimb, diaphragm, lumbar area, pelvic region, and hindlimb skeletal muscles of mdx mice, although to varying degrees in different muscle groups.[78] As a cost-saving measure, they developed their own imaging device based on LSFM to overcome the limitations of existing commercial LSFM systems, which are unable to scan large sample volumes. Through the implementation of an objective lens with a longer working distance, this system is not only compatible with a variety of chemical stains but also supports a variety of hydrophobic methods.[78]

https://doi.org/10.1021/acsomega.2c05180
ACS Omega 2023, 8, 1739−1758

Table 1. Optical Tissue-Clearing Technologies for Muscle

Method	Perfusion and Fixation	Decalcification	Delipidation	Decolorization	Dehydration	RI Matching	Others	Staining/Labeling	Final RI	Advantage	Drawback
Murray's Clear (also called BABB[a])	heparinized PBS[a]; 4% PFA[a]	EDTA[a]	gradient ethanol solution series		gradient ethanol solution series	BABB (1:2 benzyl alcohol/benzyl benzoate)		immunostaining; endogenous fluorescent protein	1.55	outstanding transparent effect; time-saving	lack of endogenous fluorescence preservation; tissue shrinkage
3DISCO[a]	heparinized PBS; 4% PFA		THF[a]; triethylamine (for pH adjustment)		THF; triethylamine (for pH adjustment)	DBE[a]		immunostaining; chemical probes; endogenous fluorescent protein;	1.56	outstanding transparent effect; time-saving	lack of endogenous fluorescence preservation; tissue shrinkage; high toxicity
CLARITY	PFA; acrylamide; bisacrylamide; VA-044[a]; PBS		SDS	SDS		FocusClear; glycerol	SDS[a] (for antigen retrieval)	immunostaining; chemical probes; endogenous fluorescent protein; FISH	1.45	efficient preservation of fluorescence, DNA[a] and RNA[a]	time-consuming; special instruments; high toxicity
simplified CLARITY method (SCM)	PBS; 4% PFA					SDS; boric acid		immunostaining; chemical probes; endogenous fluorescent protein		simple; inexpensive; easy-to-follow; portable	time-consuming
CUBIC	PBS; 4% PFA		ScaleCUBIC-1 (urea/amino alcohol/Triton X-100/NaCl)	ScaleCUBIC-1 (amino alcohol)		ScaleCUBIC-2 (urea/amino alcohol/sucrose)		immunostaining; chemical probes; endogenous fluorescent protein	1.49	hypotoxicity; inexpensive; morphological maintenance	time-consuming
FASTClear	PBS; 4% PFA		THF; SDS	SDS	THF	DBE	SDS (for antigen retrieval)	immunostaining; chemical probes	1.56	user-friendly; inexpensive	tissue shrinkage
TDE-based clearing protocol	PBS; 4% PFA					TDE		endogenous fluorescent protein		hypotoxic; relatively time-consuming; morphologically maintained	tissue shrinkage
FDISCO	PBS; 4% PFA	EDTA	THF; triethylamine (for pH adjustment)	Quadrol (selective use)	THF; triethylamine (for pH adjustment)	DBE	aluminum oxide (for peroxide removing)	immunostaining; chemical probes; endogenous fluorescent protein; virus labeling	1.56	fluorescence preservation	tissue shrinkage; incompatible with specific tracers
ScaleA2	PBS; 4% PFA					Scale A2 (urea; glycerol; Triton X-100)		immunostaining; chemical probes; endogenous fluorescent protein	1.38	fluorescence preservation	tissue expansion; increased fragility; long time for incubation; low transparency
Clear^{T2}	PBS; 4% PFA					formamide/polyethylene glycol		immunostaining; chemical probes; endogenous fluorescent protein	1.45	compatible with DiI and CTB[a]; fluorescence preservation	tissue expansion; increased fragility; long time for incubation

[a]3DISCO, three-dimensional imaging of solvent-cleared organs; BABB, benzyl alcohol and benzyl benzoate; CLARITY, clear lipid-exchanged acrylamide-hybridized rigid imaging/immunostaining/in situ hybridization-compatible tissue-hydrogel; CTB, cholera toxin subunit; CUBIC, clear, unobstructed brain imaging cocktails and computational analysis; DBE, dibenzyl ether; DNA, DNA; EDTA, ethylenediaminetetraacetic acid; FDISCO, DISCO with superior fluorescence-preserving capability; PBS, phosphate buffer saline; PFA, paraformaldehyde; RNA, ribonucleic acid; SDS, sodium dodecyl sulfate; TDE, 2,2′-thiodiethanol; THF, tetrahydrofuran; VA-044, 2,2′-azobis[2-(2-imidazolin-2-yl)propane]dihydrochloride.

https://doi.org/10.1021/acsomega.2c05180
ACS Omega 2023, 8, 1739−1758

In contrast to muscle tissue originating from a live organism, bioartificial muscles (BAMs) cultivated in vitro exhibit many distinguishing characteristics, including the absence of nourishing blood vessels and nerves, and disorganized connective tissues in the extracellular matrix. The BAM model is critical for monitoring myogenic progenitor cell differentiation and muscle fiber creation in three dimensions. Decroix et al. evaluated Sca*l*eA2, ClearT2, and 3DISCO, and found that ClearT2 had no clearing effect on isolated muscle or BAMs, while Sca*l*eA2 had a lesser clearing effect than 3DISCO.[79] Sca*l*eA2 is incompatible with antibody staining before or after clearing and is time-consuming (approximately 2 weeks).[79] Decroix evaluated the use of 3DISCO for clearing in vitro tissues and BAMs by considering the clearance effect, immunofluorescence labeling compatibility, and duration of operation. However, it should be noted that 3DISCO will linearly shrink the tissue.

McCain employed the widely used CLARITY method to clear and image tissue-engineered muscle bundles, demonstrating the 3D distribution of actin and dystrophin after immunostaining.[80] Nonetheless, it is critical to note that the tissue-clearing procedure in CLARITY may result in the destruction of tissues, which they attribute to the delipidation effect of SDS. In addition, this group is in favor of the use of CLARITY without an electric field to minimize denaturation and protein loss in tissues.[80]

3.4. Myocardium. Hsiai established cardiac LSFM (C-LSFM) for heart tissues based on the design concept of selective plane illumination microscopy (SPIM).[81] After the adult zebrafish heart was cleared by BABB, through c-LSFM imaging, they observed ventricular hypertrophy and severe trabecular degeneration in adult zebrafish after adriamycin injection.[81] Additionally, the technology can be used to image neonatal mouse hearts up to a few millimeters in diameter. To summarize, Hsiai's group employed BABB to study not only the macrostructure of the mitral and tricuspid valves but also the microscopic structure of myocardial cell fiber spiral direction, overcoming the disadvantage that microCT and other technologies are incompatible with fluorescence labeling. This appproach has a wide range of possible uses in heart development and repair.[81] Larger samples have always been a challenge for the LSFM. The concept developed by Hsiai for imaging large samples with a low-power objective lens has significantly contributed to the development of LSFM. Despite the loss of resolution, it avoids the need for a large numerical aperture objective owing to the simultaneous integration of resolution augmentation methods. Subsequently, Hsiai's group simplified and refined CLARITY via RI matching with low-cost glycerol, thus expanding the application of C-LSFM. They successfully imaged the adult mouse heart with a volume of approximately $10 \times 10 \times 10$ mm^3.[82]

Unlike Hsiai's research group, which focused on the improvement of imaging technology, Perbellini focused on the improvement of OTCT. Perbellini and colleagues refined FASTClear technology, which is free of acrylamide and sodium dodecyl benzenesulfonate. They successfully imaged and 3D reconstructed collagen fibers in myocardial slices (300 μm) from canine heart failure samples using second harmonic generation (SHG) microscopy.[55,83] Perbellini's group verified that FASTClear is compatible with isolectinB4 and Vimentin antibodies and can be used to acquire high-resolution 3D pictures of microvessels and large vessels in cardiac tissue under confocal microscopy.[55] Expanding the use of FASTClear to heart disease tissue could provide significant data support for cardiac translational research. Additionally, Sommer's group used SHG to detect fiber direction in 5 mm thick human myocardium.[84]

Along with normal cardiac tissue, Sung employed Simplified CLARITY to clear scar tissue in the hearts of mice injured by hypothermia. Their findings indicate that tdTomato+ fibroblasts express GPNMB throughout scar tissue, consistent with the immune response pathway.[85] Fischesser's group also worked on cardiac fibroblasts, demonstrating fluorescent-labeled cardiac fibroblasts throughout the mouse heart using a modified CLARITY technique.[86] Additionally, they concluded that the clearing effectiveness of passiveCLARITY was lower than that of activeCLARITY, which employs an active electrophoresis device. To minimize electrophoresis-induced protein damage, the fixing process was changed. In addition, they decolored the samples to reduce self-fluorescence.

As with H&E staining, a technique can only be considered a gold standard after it has been widely endorsed. Initially, Lee tried to utilize OTCT as a foundation for evaluating other imaging methods. This demonstrates that OTCT is rapidly gaining popularity as a dependable technology due to its precision. Lee verified diffusion tensor imaging (DTI) results obtained with CLARITY, proving capability and accuracy of DTI in mapping the orientation of cardiomyocytes. This demonstrates that DTI may also be employed for non-invasive cardiomyocyte imaging and monitoring.[87]

3.5. Myometrium. Kagami examined the uterus of nonpregnant CAG-EGFP transgenic mice using the modified CUBIC method.[88] EGFP-positive muscle cells were discovered in a network arrangement between lateral longitudinal muscle layer and medial circumferential muscle layer in the mouse uterus.[88] This layer of muscle cells was characterized as the third layer of muscle cells in the myometrium. This layer is dense with blood vessels and tubulin-3-positive nerve axons and shows a reticular arrangement of muscle cells. Telocytes in this layer are in contact with nerve axons, suggesting that telocytes can transmit signals from the nervous system to the muscular layer.[88] To be certain, no alterations in tissue morphology were seen in the experiment due to CUBIC. The CUBIC protocol is suitable for the myometrium since it removes more pigment and preserves the sample profile.

A detailed description of the optical tissue-clearing techniques used in muscle tissues can be found in Table 1.

4. BONE AND BONES

4.1. Transparent Cranial Window. Early imaging of cortical veins is often accomplished by cranial surgery,[89] such as skull removal, a cranial window, and a thinning-skull cranial window. However, craniocerebral damage produced by surgical trauma may cause the observed cortical vasculature to vary from the real condition, compromising accuracy and reliability. Zhu's team evaluated a vast number of chemical reagents to tackle this issue. They then proposed a novel method of tissue-clearing called skull optical clearing solution (SOCS).[90] SOCS is a combination of several reagents, among which lauryl alcohol and sodium dodecyl benzenesulfonate are effective delipidators; saturated glucose solution and dimethyl sulfoxide improve SOCS penetration; and sorbitol with a high RI matches the RI of samples.[90] All processes used SOCS reagent. SOCS not only promotes optical clearing of the skull in vitro, but can also be used to image the skull in mice in vivo. SOCS, when combined with laser speckle technology and photo-

https://doi.org/10.1021/acsomega.2c05180
ACS Omega 2023, 8, 1739−1758

acoustic microscopy imaging technology, enables imaging of intact mouse cerebral microvessels and blood flow in vivo.[89] The fact that the safety of in vivo imaging was not adequately demonstrated may explain why this approach has not received sufficient attention since its introduction. Additionally, SOCS has not been demonstrated to facilitate high-resolution imaging of cortical nerves nor has it been demonstrated to prevent damage to fluorescent proteins or to be compatible with exogenous dyes. Hence, Zhu's group proposed USOCA (not an abbreviation) based on SOCS. USOCA can also be used in vivo, similar to SOCS. By cleaning the transparent region with PBS, the skull is returned to its normal state, indicating that USOCA can be used to observe chronic disorders. Unlike SOCS, USOCA is not affected by mouse age. It is capable of producing efficient transparency for mouse skulls of various chemical compositions and ages, and its safety has been established.[91] Laser speckle contrast imaging (LSCI) and hyperspectral imaging (HSI) are used to create a dual-mode optical imaging system.[91,92] HIS measures oxygen saturation, whereas LSCI assesses cerebral blood flow. USOCA enhances the contrast and resolution of cerebral blood flow and oxygen saturation maps within this imaging system. USOCA overcomes the inability of SOCS to be used for imaging the nervous system. Using immunohistochemical labeling of CX3Cr1-GFP mice and anti-GFAP antibodies, it was shown that mice treated with USOCA for 2 days did not exhibit pathological inflammation.[91] Currently, USOCA reagents only allow structural imaging of the skull but not functional imaging. Fortunately, Zhu's study team verified that the long-term effects of USOCA on cortical microvessels are harmless. Although microglial cell dynamics were considered with USOC, the monitoring period was not long enough to determine if long-term use of USOCA would cause changes in the structure of cortical neurons in other ways.

Zhu developed the VNSOCA (visible-NIR-II-compatible skull optical clearing agents) clearing reagent by substituting deuteroxide for water as the USOCA solvent. Near-infrared (NIR) light provides an advantage over visible light for imaging deep tissues, particularly at NIL-II, because tissue scattering reduces with wavelength (900−1700 nm). However, NIR-II cannot be paired with OTCT because the water used in conventional OTCTs exhibits high absorption at wavelengths longer than 1300 nm. The VNSOCA reagent permits not only NIR-II excitation light to pass through the skull but also visible signal light. It can also be used to image excited NIL-II using third harmonic generation (THG) microscopy.[93] However, VNSOCA can induce optical damage in individual capillaries.[93]

SOCS-related techniques do not necessarily involve the application of OTCTs to skeletal muscle systems. Instead, the ultimate goal of applying these approaches is to obtain high spatiotemporal resolution imaging of the cerebral cortex microcirculation system, glial cells, and other structures. They are also included because these techniques are the first to render the musculoskeletal system transparent in vivo, which is of critical importance.

4.2. Alveolar Bone and Dental Implants. PEGASOS was utilized by Zhao's group to address the challenge of 3D imaging of the implant−bone interface. Prior to applying OTCT to the alveolar bone−implant interface, 3D imaging of the alveolar bone−implant interface could only be achieved by μCT. However, owing to metal halo artifacts,[94] microCT could not discriminate the alveolar bone−implant interface and could not be used to observe the cell composition and fluorescence signals. By using PEGASOS, Zhao's group not only successfully achieved 3D imaging of the alveolar bone−implant interface but also found that successful angiogenesis after implant implantation did not guarantee successful osteogenesis.[95] The comparison of μCT and SHG signals in the same targeted area showed that the decalcification step in PEGASOS will not affect the alveolar bone−implant interfaces.[95] For incompatible decalcification staining techniques, they observed that PEGASOS without decalcification could also produce 3D imaging of calcein green labeling paired with endogenous fluorescence, but the imaging depth was proportionally decreased (~350 μm).[95] Using tracing technology combined with PEGASOS, Zhao's team performed 3D imaging of bone integration after tooth extraction and delayed implantation in mice. The results showed that Gli1+ cells in alveolar bone proliferated after tooth extraction and were closely connected to blood vessels throughout the process.[96] In transgenic mice with specific Gli1+ cell knockdown, the researchers found that Gli1+ cells were required for peri-implant osteogenesis, a process that may be mediated by the Wnt pathway.[96] Additionally, LepR antibody immunostaining revealed that LepR+ cells may arise from Gli1+ cells after tooth extraction.[96,97]

4.3. Long Bone Cortical Vessels. The team of Gunzer coupled modified simpleCLEAR with a number of optical imaging techniques such as confocal microscopy, scanning electron microscopy, light microscopy, and X-ray microscopy, to create a 3D picture of mouse long bones (femur and tibia). In the bone cortex of mice, numerous microvascular structures known as transcortical capillaries were discovered.[98] Researchers also found similar structures in the phalanges, skulls, and femurs of mice treated with simpleCLEAR.[98] This work not only expands the application scope of simpleCLEAR but also located and labeled transcortical vessels for the first time. This discovery demonstrates the significance of 3D imaging in scientific studies.

3D imaging provides a spatial position relationship that is difficult to depict in 2D imaging and serves as a solid foundation for reliable conclusions. Cai et al. combined transgenic mice with vDISCO in the same year. They discovered a similar structure in the skulls of mice, which they dubbed short skull meningeal connections (SMCs). It is not known if these vessels are lymphatic or vascular due to a lack of relevant reporting mice. It has been shown that VEGFR3+ arteries stretch from the meninges into the cortex of the skull and carry LysM GFP+ immune cells.[56] This technique makes use of nanoantibodies coupled with a strong fluorescent dye to multiply the fluorescence signal by a factor of 100. Due to the significant autofluorescence of skeletal muscle, vDISCO has promising future uses in this system.

4.4. Craniofacial Bone Development. Zhao's team expanded the application of PEGASOS by combining it with transgenic mice. They discovered that osteogenic activity and vascular density were widespread throughout the skull during the first 2 weeks after birth. However, the osteogenic activity and vascular density decreased and gathered in the bone suture area and bone marrow space after 2 weeks.[99] Suture mesenchymal stem cells (SuMSCs) are can be labeled with antibodies against Gli1 or Axin2. Elimination of SuMSCs causes suture fusion. In addition, Gli1+ mesenchymal stem cells were found localized near blood arteries in craniofacial bone, similar to the findings in long bone.[99] This conclusion contradicts the conclusion that SuMSCs are independent of

https://doi.org/10.1021/acsomega.2c05180
ACS Omega 2023, 8, 1739−1758

the blood vessels in the skull, which is usually drawn from two-dimensional imaging.

4.5. Bone Marrow. Using uDISCO, Pan et al. studied the location of bone marrow mesenchymal stem cells in whole mice without decalcification. In this study, quantum-dot-labeled BMSCs from β-actin EGFP mice were detected in the bone marrow and intestinal tract of C57BL/6 mice.[40] Using BABB in conjunction with immunolabeling, Gorelashvili et al. discovered that the quantity and size of megakaryocytes in two-dimensional images were severely underestimated.[100] Additionally, different types of bone marrow cells may be analyzed using OTCT. The Greenbaum group used Bone CLARITY technology to obtain an image depth of approximately 1.5 mm in the epiphysis of long bones and mapped the spatial distribution of bone progenitor cells. A substantial increase in the number of Sox9+ cells were detected in Sox9CreER transgenic mice after subcutaneous injection of sclerostin antibody (scl-AB), showing that more bone progenitor cells may be recruited to the bone surface and contribute to an increase in the osteoblast population.[101]

In addition, 2ECi (second generation ethyl cinnamate based clearing method),[102] SeeDB,[103] and other technologies also achieved clearing of the skeleton. Among them, SeeDB can only image 10−40 μm below the surface of intact cortical bone in mouse femurs. Currently, there are only a few studies on the use of these techniques. In addition, there is a lack of data support for the clearing effect of other bones and muscles beyond the research objectives.

A detailed description of the optical tissue-clearing techniques used in bones can be found in Table 2.

5. CARTILAGE

Due to the limited development of optical imaging technologies in the past, OTCT was rarely used for cartilage.

Generally, it is believed that the meniscus is a tissue structure devoid of blood supply; therefore, the presence of an adequate vascular supply is considered an influential factor in meniscus healing. However, early studies of meniscus vascular structures have been rather sparse. In several studies, using modified Spalteholz, the microvascular anatomy of articular cartilage has been elucidated more thoroughly. Also using modified Spalteholz, Arnoczky and Warren discovered that the posterolateral side of the lateral meniscus lacks blood flow due to its connection with the popliteus tendon, which indicates that lesions on this side of the meniscus are more difficult to cure.[104] They studied the effects of synovial and capsular tissues around the joint in postoperative joint reconstruction using a canine articular disc. Furthermore, they discovered that wounds within the peripheral, vascular-rich meniscus may heal and cause fibrovascular scarring. However, longitudinal incisions in the area of the meniscus devoid of blood vessels failed to heal.[105] In a later work, Arnoczky et al. used this approach to demonstrate that tears around the triangular-fibrochondral complex may be reparable. A tear that occurs in the center and along the tibial attachment is less likely to heal.[106] Crawford et al. evaluated the depth of medial and lateral meniscus blood supply in young and elderly people[107] using Arnoczky's modified Spalteholz method. The modified Spalteholz method described in this study was based on the method proposed by Crawford.[107] A detailed introduction of this technology requires further study of the suggested literature.[108] Previously, due to the limitations of imaging technology, this approach has only been utilized to enhance the vascular structure of articular disc cartilage and to visualize cartilage slices under a microscope. It is only possible to perform imprecise quantitative analyses of the microvessels in articular cartilage. Moreover, this approach is time-consuming, needing approximately 8−9 days to obtain clearing the 5 mm meniscus.[107]

With recent advancements in data processing and imaging technology, OTCT has been used to study cartilage at the cellular level. SeeDB was utilized by Calve's group to discover intercellular connections embedded in the thick, mineralized extracellular matrix.[103] Confocal imaging demonstrated that cellular connections might extend beyond the pericellular matrix, lending credence to the presence of chondrocyte connections.[103] Neu's group achieved transparency of cartilage approximately 2.5 mm thick using SeeDB.[24] The imaging depth is primarily restricted by the working distance of the objective when utilizing typical confocal (single-photon) fluorescence imaging. Neu et al. discovered intercellular connections in the load-bearing area of cartilage tissue, indicating that cell connections play a role in stress distribution.[24] Using cryogenic scanning electron microscopy, they concluded that SeeDB had no effect on the morphology or ultrastructure of tissues. In accordance with the Calve group's proposal, Neu discovered that tiny molecules, such as Hechst, Dil, and photoleptide, may permeate the cartilage matrix, and hence small molecular antibodies should be utilized when immunofluorescence labeling is used in cartilage.[24] SeeDB offers essential benefits in cartilage research due to its ability to maintain sample morphology. However, it should be highlighted that the final transparency of large samples is not acceptable, even with prolonged treatment time, due to the lack of delipidation. Although raising the temperature may successfully improve osmotic impact, it must be done at the expense of increasing self-fluorescence and quenching of target fluorescent proteins. Furthermore, although SeeDB is compatible with a wide range of fluorescent probes, the time and cost rise with the size and amount of antibodies applied,[103] undermining SeeDB's touted benefits of being rapid, simple, and inexpensive. Furthermore, SeeDB was shown to have little to no clearing impact in the articular disc and ligaments.[103]

Omnipaque is a water-soluble, non-ionic radiocontrast agent that is extensively used in angiography and arthrography.[109] According to Bykov et al., Omnipaque can optically clear articular cartilage tissue. Omnipaque can be used to image bovine articular cartilage via optical coherence tomography (OCT) and to correctly define the chondro−bone interface.[109,110] Furthermore, this research group attempted to employ glycerin and fructose for the treatment of hyaline cartilage based on nIR imaging,[111] but the glycerin and fructose concentrate was highly permeable and induced high permeable stress in chondrocytes and significant changes in tissue morphology. It was found that using Omnipaque to help modify costal cartilage autografts can raise the maximum temperature during infrared irradiation and is chemically stable under the infrared laser used in the clinic.[112] The explanation regarding the Omnipaque clearing procedure provided by Bykov's group was insufficient for comparison with other methods that may be used in cartilage. Furthermore, the compatibility of the technique with endogenous fluorescent protein and exogenous dye has not been confirmed, and therefore, the technique has limited guiding value for applications other than OCT and infrared laser treatment.

https://doi.org/10.1021/acsomega.2c05180
ACS Omega 2023, 8, 1739−1758

Table 2. Optical Tissue-Clearing Technologies for Bone

Method	Perfusion and Fixation	Decalcification	Delipidation	Decolorization	Dehydration	RI Matching	Others	Staining/Labeling	Final RI	Advantage	Drawback
modified Murray's Clear (also called BABB[a])	heparinized PBS; 4% PFA[a]	EDTA[a]	gradient ethanol solution series		gradient ethanol solution series	BABB (1:2 benzyl alcohol/ benzyl benzoate)		compatible	1.55	outstanding transparent effect; time-saving	lack of endogenous fluorescence preservation
3DISCO[a]	heparinized PBS; 4% PFA		THF[a]; triethylamine (for pH adjustment)		THF; triethylamine (for pH adjustment)	DBE[a]		immunostaining; chemical probes; endogenous fluorescent protein	1.56	outstanding transparent effect; time-saving	lack of endogenous fluorescence preservation; tissue shrinkage; high toxicity
uDISCO[a]	heparinized PBS; 4% PFA		*tert*-butanol		*tert*-butanol	diphenyl ether mixed with BABB (BABB-D)		compatible (also compatible with virus labeling)	1.579	high preservation capacity of fluorescent protein; long-term preservation and imaging	unconfirmed isotropic shrinkage in muscle
vDISCO[a]	heparinized PBS; 4% PFA	EDTA and amino alcohol	DCM[a]	CUBIC-1 (urea; Triton X-100; Quadrol)	THF	BABB	permeabilization solution (Triton X-100, methyl-β-cyclodextrin (extract cholesterol), *trans*-1-acetyl-4-hydroxy-L-proline (loosen the collagen)	immunostaining; chemical probes; endogenous fluorescent protein	1.56	robust fluorescence intensity; long-term preservation and imaging	time-consuming; high cost
bone CLARITY	heparinized PBS; 4% PFA	EDTA	8% SDS[a]	25% Quadrol		Histodenz[66]	hydrogel embedding 4% acrylamide, 0% PFA, and 0.25% thermoinitiator (VA-044[a])	immunostaining; chemical probes; endogenous fluorescent protein	1.47	high preservation capacity of fluorescent protein	time-consuming
PEGASOS[a]	heparinized PBS; 4% PFA	20% EDTA	tB	25% Quadrol	tB-PEG[a] (70% (v/v) *tert*-butanol, 27% (v/v) PEG methacrylate Mn 500 (PEGMMA500))	BB-PEG[a] (75% (v/v) benzyl benzoate (BB), 25% (v/v) PEGMMA500, 3% (w/v) Quadrol)		immunostaining; chemical probes; endogenous fluorescent protein	1.543	high transparency; preservation endogenous GFP[a] fluorescencet	tissue deformation; high autofluorescence (muscle)
SOCS[a]		SOCS(EDTA)	SOCS (laurinol; sodium dodecyl benzenesulfonate)		SOCS (laurinol; glucose solution)	SOCS (sorbitol)			1.426	compatible with in vivo experiment; hypotoxicity; reversibility	narrow scope of application; untested safety
USOCA[a]			USOCA-S1 (ethanol)		USOCA-S1 and -S2 (ethanol; sodium dodecyl benzenesulfonate)	USOCA-S1 (urea)			1.396−1.402	compatible with in vivo experiment; hypotoxicity; reversibility	narrow scope of application
VNSOCA[a]			VNSOCA-S1 (ethanol)		VNSOCA-S1 and -S2 (ethanol; sodium dodecyl benzenesulfonate)	VNSOCA-S1 (urea)			1.396−1.402	compatible with in vivo experiment; compatiblewith NIR-II exciation light; hypotoxicity; reversibility	narrow scope of application

https://doi.org/10.1021/acsomega.2c05180
ACS Omega 2023, 8, 1739−1758

Table 2. continued

Method	Perfusion and Fixation	Decalcification	Delipidation	Decolorization	Dehydration	RI Matching	Others	Staining/Labeling	Final RI	Advantage	Drawback
simple CLEAR/ Eci	heparinized PBS; 4% PFA		ethanol (pH 9.0)		ethanol (pH 9.0)	Eci[a]		immunostaining; chemical probes; endogenous fluorescent protein	1.559−1.561	hypotoxicity; economical; fluorescence preservation	relatively poor transparency effect
2Eci-[a]	PBS; 4% PFA		1-propanol (pH 9.0)	3% H_2O_2; 0.5% KOH	1-propanol (pH 9.0)	Eci		immunostaining; chemical probes; endogenous fluorescent protein	1.559−1.561	hypotoxicity; fluorescence preservation;	relatively poor transparency effect
SeeDB[a]	4% PFA					SeeDB (80.2 (w/w) fructose); SeeDB37 (86.7 (w/w) fructose)		endogenous fluorescent protein	1.490−1.502	morphology-preserving; easy to learn; inexpensive; safe; quick	not suitable for large samples; Maillard reaction; viscosity increment

[a]BABB, benzyl alcohol and benzyl benzoate; PBS, phosphate buffer saline; PFA, paraformaldehyde; EDTA, ethylene diamine tetraacetic acid; 3DISCO, three-dimensional imaging of solvent-cleared organs; THF, tetrahydrofuran; DBE, dibenzyl ether; uDISCO, ultimate DISCO; vDISCO, variable domain of heavy chain antibodies (nanobodies) DISCO; DCM, dichloromethane; VA-044, 2,2′-azobis[2-(2-imidazolin-2-yl)propane]dihydrochloride; PEGASOS, polyethylene glycol (PEG)-associated solvent system; tB, *tert*-butanol; tB-PEG, 70% (v/v) *tert*-butanol, 27% (v/v) PEG methacrylateMn500 (PEGMMA500), and 3% (w/v) Quadrol; BB-PEG, 75% (v/v) benzyl benzoate (BB), and 25% (v/v) PEGMMA500 and Quadrol; GFP, green fluorescent protein; SOCS, skull optical clearing solution; USOCA, not an abbreviation; VNSOCA, visible-NIR-II-compatible skull optical clearing agents; Eci, Ethyl cinnamate; 2Eci, second generation ethyl cinnamate based clearing method; SeeDB, see deep brain.

However, it is worth noting that Omnipaque is a hypotonic clearing reagent/contrast agent with minimal effect on cartilage shape and structure, making it a potentially reliable reagent cartilage.

Since cartilage is structurally heterogeneous, certain OTCTs that result in morphological changes must be carefully considered before being used for cartilage-related research which requires high degrees of local and structural precision. For instance, some hydrophilic tissue-clearing techniques, such as PEGASOS, result in substantial tissue contraction. Thus, it is still imperative to establish a new protocol for cartilage research that does not affect tissue morphology and ultrastructure.

A detailed description of the optical tissue-clearing techniques used in cartilage can be found in Table 3.

6. LIGAMENTS AND TENDONS

Ligaments and tendons have received less attention than cartilage, bone, and muscle. As vital elements of the musculoskeletal system, ligaments and tendons stimulate movement by transmitting muscle force to bones. Arnoczky's group photographed the microvascular supply of the lateral epicondyle and extensor muscle using a modified Spalteholz method and an injection of Indian ink and discovered that the lateral epicondyle area had two hypovascular zones. The first is proximal to the lateral epicondyle, and the second is 2−3 cm proximal to the lateral epicondyle.[113] These vascularized patches may impede local wound healing and promote inflammation, suggesting that they are the source of humeral external epicondylar irritation.[113]

Yi Feng's team imaged blood arteries, neurons, and nuclei in the quadriceps tendon using passive CLARITY technology.[71] Passive CLARITY was shown to be compatible with immunomarkers and capable of achieving transparency in tendons rich in fibrous tissue.

7. 3D IMAGING ACQUISITION

7.1. Laser Scanning Confocal Microscope. A confocal microscope offers the advantage of using a high-quality laser as the light source and minimizing interference beyond the focusing plane through spatial filtering, thereby greatly improving contrast and resolution. In contrast to LSFM, its point-scanning properties mean that its imaging speed is modest, and it is more susceptible to photobleaching and phototoxicity. Existing technology, such as resonance scanners, is attempting to accelerate imaging. The use of confocal microscopy is highly recommended for imaging and examining tiny areas of tissues at high resolution.

7.2. Two-Photon Microscope. Femtosecond laser-based two-photon microscopy employs longer wavelengths than those of confocal microscopy, so photons penetrate deeper and are less cytotoxic. Two-photon microscopy has inferior lateral and axial resolution and low-speed imaging due to point-by-point scanning.[79] Absorbing two photons at the same time means that only the focal point can be excited, so no tissue outside the focal point can be damaged. An obvious advantage of the two-photon microscope is its compatibility with the second harmonic signal. Second harmonic imaging is a nonlinear optical imaging method. Collagen fibers abundant in the musculoskeletal system have strong second harmonic signal, and different types of collagen fibers have different signals.[114]

https://doi.org/10.1021/acsomega.2c05180
ACS Omega 2023, 8, 1739−1758

Table 3. Optical Tissue-Clearing Technologies for Cartilage

Method	Perfusion and Fixation	Decalcification	Delipidation	Dehydration	RI Matching	Staining/Labeling	Final RI	Advantage	Drawback
modified Spalteholz	10% neutral-buffered formalin	10% nitric acid	chloroform	ethanol (70%, 95%, 100%)	Spalteholz solution (3:5 benzyl benzoate/methyl salicylate)			basis for other protocols	time-consuming
SeeDB[a]	4% (w/v) PFA[a]				SeeDB (80.2 (w/w) fructose); SeeDB37 (86.7 (w/w) fructose)	compatible with various neuronal tracers (including DiI)	1.490−1.502	morphology-preserving; easy to learn; inexpensive; safe; quick	not suitable for large samples; Maillard reaction
Iohexol	PBS[a] and frozen at −20 °C				Iohexol		1.501− 1.519	clinical utility	limited application

[a]PBS, phosphate buffer saline; PFA, paraformaldehyde; SeeDB, see deep brain.

7.3. Light-Sheet Fluorescence Microscope. LSFM scans the sample plane by plane, not point by point. And the LSFM transmits an ultrathin light sheet through the tissue, with the illumination perpendicular to the direction of detection. Initially, LSFM was primarily used for the imaging of tiny and transparent samples (zebrafish). With the advent of OTCT, it may be used for much larger and more opaque samples.[115] Because the tissues above and below the light sheet are not stimulated, LSFM provides superior axial resolution and scanning speed, as well as reduced photobleach and phototoxicity.[10] At present, there are a variety of commercially available LSFMs. Some researchers have also developed customized LSFMs based on the original design proposal of LSFM in order to maximize cost effectiveness and meet specialized research needs. The major purposes are to enhance the working distance, the resolution, the use of dual illumination to compensate for the non-uniformity of large volume lighting, etc.

7.4. SHG Microscopy. The imaging principle of SHG is principally based on a second-order nonlinear effect. The SHG microscope is created by modifying the two-photon microscope. As a result, it has properties similar to the two-photon microscope but also offers many advantages. First, no additional staining is needed for SHG microscopy, and since there is no energy absorption in the imaging process, phototoxicity and photobleaching effects are mostly avoided in samples. Because the SHG may collect signals in reverse, it can be seen simultaneously with two-photon microscopy and other imaging modalities. SHG has a higher signal-to-noise ratio than fluorescence imaging. The SHG microscope has a broad application prospect in the musculoskeletal system since collagen fibers are rich in bones, tendons, muscles and cartilage.

8. CONCLUSION

Since OTCT is experiencing rapid growth, its development goals should not be restricted to expanding the range of application and improving the clearing effect. In contrast, we should focus on enhancing the ability to retain endogenous fluorescent proteins, safeguard antigen integrity, maintain tissue morphological stability, and ensure reagent safety. Currently, there are few specific methods designed for the musculoskeletal system. Some researchers have modified existing OTCTs to better accommodate the musculoskeletal system. For example, Verma et al. integrated and modified CUBIC, iDISCO, and Sca*l*eS so that they could be used to study skeletal muscle in adult mice. However, these methods can only efficiently clear small samples, such as testicular muscle.[116] Friedrich developed and enhanced a tissue-clearing method for the musculoskeletal system based on TDE.[77] At present, there are a limited number of OTCTs for the musculoskeletal system, and the majority of the studies utilize published techniques or their modifications.[72]

Considering the current applications of OTCT in the musculoskeletal system, we proposed that researchers should be aware that there is no method that is applicable to multiple tissues or research purposes. The best optical tissue-clearing approach is the result of careful consideration based on the experimental goal, budget, facilities and subject.

When using OTCTs in the musculoskeletal system, researchers must consider the following: (1) The fluorescent proteins used today (EGFP, EYFP, mCherry, etc.) mainly emit light and are detected in the visible spectrum. Nevertheless,

https://doi.org/10.1021/acsomega.2c05180
ACS Omega 2023, 8, 1739−1758

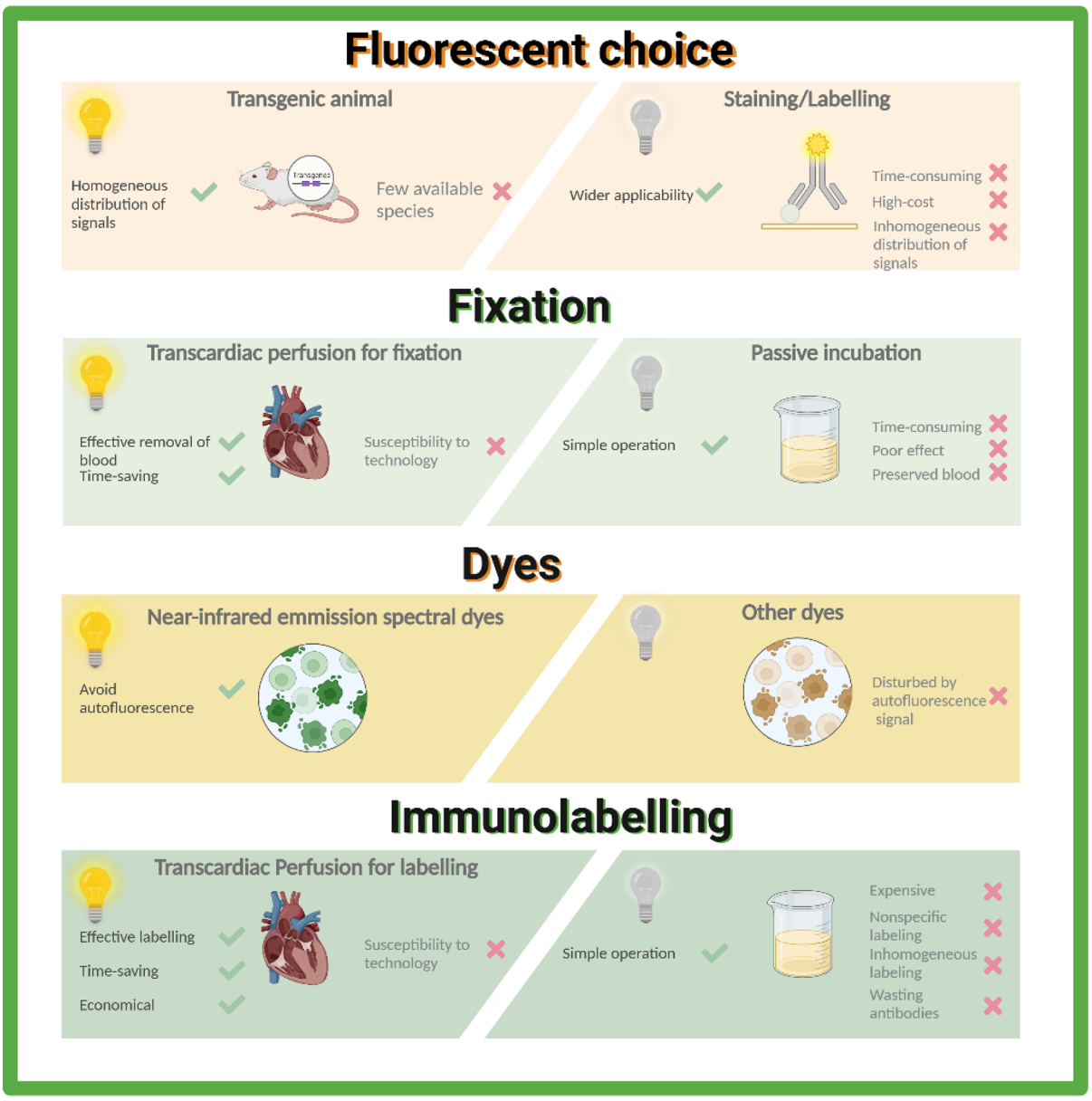

Figure 3. Recommended methods for musculoskeletal system.

bone and muscle exhibit self-fluorescence due to high levels of heme[114], which impedes the observation of target fluorescence. In the processes of sample perfusion and fixation, we recommend using cardiac perfusion to preliminarily remove a substantial volume of blood. We recommend further decolorization of samples after cardiac perfusion due to the limited efficacy of cardiac perfusion. (2) When choosing between transgenic fluorescent reporter mice and immunostaining, we suggest using fluorescence reporter mice. Immunostaining cannot guarantee a homogeneous distribution of signals in large samples and may substantially lengthen the experimental period. In addition, large samples can significantly increase immunostaining costs. However, immunostaining offers some benefits in certain situations. In reporter mice, may be destroyed when tissues are cleared, and they may also be obscured by surrounding autofluorescence. In this case, immunolabeling of the sample is preferable. In addition, the transgenic technique is not applicable if the study object is primate or human tissue. (3) For immunolabeling, we advocated in vivo infusion/intravenous injection rather than in vitro passive incubation. Due to the specific structure of bone, in vitro passive incubation often necessitates long incubation times. Moreover, immersion for long periods of time can still lead to uneven antibody distribution and nonspecific fluorescence accumulation.[100] By dividing bone in half, the issue of a lengthy incubation time can be resolved (when tissue integrity is not required). In terms of antibody choice, we recommend antibodies that have a small volume for quick penetration, such as the nanoantibodies used in vDISCO. (4) To prevent interference with the detection of target fluorescence caused by tissue self-fluorescence in the shorter wavelength range of visible light, it is recommended to employ dyes that emit near-infrared light. Commonly used dyes, such as Alexa Fluor 488 and Alexa Fluor 555, are difficult to observe owing to the self-fluorescence of muscles. For the fluorescent reporter mice, the spectra can also be red-shifted using antifluorescent protein antibodies.[116] (5) The use of EDTA for decalcification has not yet been shown to affect the

https://doi.org/10.1021/acsomega.2c05180
ACS Omega 2023, 8, 1739−1758

macroscopic or microscopic structure of bone. Therefore, we propose decalcification for research with high bone transparency requirements. (6) Although some studies indicate that the shrinkage resulting from certain methods is isotropic,[40] the majority of presently used hydrophilic tissue-clearing methods result in visible shrinkage of samples. For research that requires a high level of tissue morphological precision, we suggest methods with fewer effects on sample shape. Thus, minor shrinkage may be addressed with a simple scaling of the picture. We do not advocate employing OTCTs that result in nonlinear shrinkage. (7) The direct application of SHG microscopy imaging of unlabeled samples allows quantitative analysis and 3D visualization of second harmonic-sensitive proteins, such as collagens, in bones, and muscles. (8) The transparent cranial window technique has been applied in vivo, but this achievement is not sufficient to demonstrate that this technology may be widely used in other tissues. Because the skull is rich in collagen and hydroxyapatite, it contains very few cell components. The adoption of this approach to in vivo imaging requires careful thought (Figure 3).

The selection of tissue-clearing methods should take into account the penetration effect, tissue deformation, and clearing effect, since the musculoskeletal system contains abundant inorganic components, blood, and fibrillar connective tissue.

Due to its unique composition and structure, it is vital to create specialized OTCTs suited to studying the musculoskeletal system. The key characteristics of such a method would be as follows: (1) Since muscles may exhibit strong self-fluorescence in the visible light spectrum following PFA fixation, it is necessary to screen NIR dyes that may be utilized for labeling or further screen-fixed reagents that can lower the self-fluorescence intensity. (2) The volumes of bones and muscles are greater than that of other tissues. However, LSFM systems with large numerical apertures are restricted in their working distance, which makes bulk sample imaging difficult. Accordingly, objective and high-resolution imaging algorithms for the musculoskeletal system are in increasing demand. (3) Due to the size of muscles and bones, a greater number of clearing reagents is needed to achieve transparency compared to other tissues, and further lowering the toxicity of reagents is an urgent and essential aim in this area. (4) For high-resolution imaging of musculoskeletal systems, techniques for automated monitoring and counting of cells or cell-level structures (such as neuromuscular junctions) are needed. (5) As the structure of musculoskeletal tissues is evidently heterogeneous, accurate tissue morphology is often required in relevant research. Therefore, we need a method that can guarantee the transparency effect without affecting the morphology of the tissue.

For instance, the newly developed NeuroGPS-Tree algorithm provides a potent method for autonomous neuron tracking.

AUTHOR INFORMATION

Corresponding Author

Nan Jiang − *State Key Laboratory of Oral Diseases & National Clinical Research Center for Oral Diseases, West China Hospital of Stomatology, Sichuan University, Chengdu 610041, China; West China Hospital of Stomatology, Sichuan University, Chengdu 610041, China;* orcid.org/0000-0001-9221-9568; Email: dent_jn@163.com

Authors

Yan-Jing Zhan − *State Key Laboratory of Oral Diseases & National Clinical Research Center for Oral Diseases, West China Hospital of Stomatology, Sichuan University, Chengdu 610041, China*

Shi-Wen Zhang − *State Key Laboratory of Oral Diseases & National Clinical Research Center for Oral Diseases, West China Hospital of Stomatology, Sichuan University, Chengdu 610041, China; West China Hospital of Stomatology, Sichuan University, Chengdu 610041, China*

SongSong Zhu − *State Key Laboratory of Oral Diseases & National Clinical Research Center for Oral Diseases, West China Hospital of Stomatology, Sichuan University, Chengdu 610041, China; West China Hospital of Stomatology, Sichuan University, Chengdu 610041, China*

Complete contact information is available at: https://pubs.acs.org/10.1021/acsomega.2c05180

Funding

This work was supported by grants from the National Natural Science Foundation of China (No. 81901026) and the Department of Science and Technology of Sichuan Province (No. 2021YFH0139).

Notes

The authors declare no competing financial interest.

ACKNOWLEDGMENTS

The authors acknowledge Biorender that is used to create Figures 1−3 and publication certification has achieved from Biorender.com.

REFERENCES

(1) World Health Organization. *Musculoskeletal conditions*. https://www.who.int/news-room/fact-sheets/detail/musculoskeletal-conditions (accessed July 14, 2022).

(2) World Health Organization. Musculoskeletal conditions affect millions. https://www.who.int/news/item/27-10-2003-musculoskeletal-conditions-affect-millions.

(3) Hughes, L.; Hawes, C.; Monteith, S.; Vaughan, S. Serial block face scanning electron microscopy–the future of cell ultrastructure imaging. *Protoplasma* **2014**, *251* (2), 395−401.

(4) Pinali, C.; Kitmitto, A. Serial block face scanning electron microscopy for the study of cardiac muscle ultrastructure at nanoscale resolutions. *J. Mol. Cell Cardiol.* **2014**, *76*, 1.

(5) Goggin, P.; Ho, E. M. L.; Gnaegi, H.; Searle, S.; Oreffo, R. O. C.; Schneider, P. Development of protocols for the first serial block-face scanning electron microscopy (SBF SEM) studies of bone tissue. *Bone* **2020**, *131*, No. 115107.

(6) Moser, E.; Stadlbauer, A.; Windischberger, C.; Quick, H. H.; Ladd, M. E. Magnetic resonance imaging methodology. *Eur. J. Nucl. Med. Mol. Imaging* **2009**, *36* (S1), 30−41.

(7) Grinolds, M. S.; Warner, M.; De Greve, K.; Dovzhenko, Y.; Thiel, L.; Walsworth, R. L.; Hong, S.; Maletinsky, P.; Yacoby, A. Subnanometre resolution in three-dimensional magnetic resonance imaging of individual dark spins. *Nat. Nanotechnol.* **2014**, *9* (4), 279−284.

(8) Xu, J.; Jiang, X.; Devan, S. P.; Arlinghaus, L. R.; McKinley, E. T.; Xie, J.; Zu, Z.; Wang, Q.; Chakravarthy, A. B.; Wang, Y.; Gore, J. C. MRI-cytometry: Mapping nonparametric cell size distributions using diffusion MRI. *Magn. Reson. Med.* **2021**, *85* (2), 748−761.

(9) Jones, C. W.; Smolinski, D.; Keogh, A.; Kirk, T. B.; Zheng, M. H. Confocal laser scanning microscopy in orthopaedic research. *Prog. Histochem. Cytochem.* **2005**, *40* (1), 1−71.

(10) Hillman, E. M. C.; Voleti, V.; Li, W.; Yu, H. Light-sheet microscopy in neuroscience. *Annu. Rev. Neurosci.* **2019**, *42*, 295−313.

(11) Bush, P. G.; Wokosin, D. L.; Hall, A. C. Two-versus one photon excitation laser scanning microscopy: critical importance of excitation wavelength. *Front. Biosci.* **2007**, *12*, 2646−2657.
(12) Spalteholz, W. Über das Durchsichtigmachen von menschlichen und tierischen Präparaten und seine theoretischen Bedingungen, nebst Anhang. 1914.
(13) Almagro, J.; Messal, H. A.; Zaw Thin, M.; van Rheenen, J.; Behrens, A. Tissue clearing to examine tumour complexity in three dimensions. *Nat. Rev. Cancer* **2021**, *21* (11), 718−730.
(14) Ueda, H. R.; Ertürk, A.; Chung, K.; Gradinaru, V.; Chédotal, A.; Tomancak, P.; Keller, P. J. Tissue clearing and its applications in neuroscience. *Nat. Rev. Neurosci* **2020**, *21* (2), 61−79.
(15) Jing, D.; Yi, Y.; Luo, W.; Zhang, S.; Yuan, Q.; Wang, J.; Lachika, E.; Zhao, Z.; Zhao, H. Tissue clearing and its application to bone and dental tissues. *J. Dent. Res.* **2019**, *98* (6), 621−631.
(16) Oliveira, L. M.; Carvalho, M. I.; Nogueira, E. M.; Tuchin, V. V. Diffusion characteristics of ethylene glycol in skeletal muscle. *J. Biomed. Opt.* **2015**, *20* (5), No. 051019.
(17) Carneiro, I.; Carvalho, S.; Henrique, R.; Oliveira, L. M.; Tuchin, V. V. A robust ex vivo method to evaluate the diffusion properties of agents in biological tissues. *J. Biophotonics* **2019**, *12* (4), No. e201800333.
(18) Tainaka, K.; Kuno, A.; Kubota, S. I.; Murakami, T.; Ueda, H. R. Chemical principles in tissue clearing and staining protocols for whole-body cell profiling. *Annu. Rev. Cell Dev. Biol.* **2016**, *32*, 713−741.
(19) Yu, T.; Zhu, J.; Li, D.; Zhu, D. Physical and chemical mechanisms of tissue optical clearing. *iScience* **2021**, *24* (3), No. 102178.
(20) Clarke, B. Normal bone anatomy and physiology. *Clin. J. Am. Soc. Nephrol.* **2008**, *3* (Suppl 3), S131−S139.
(21) Florencio-Silva, R.; Sasso, G. R. D. S.; Sasso-Cerri, E.; Simões, M. J.; Cerri, P. S. Biology of bone tissue: structure, function, and factors that influence bone cells. *Biomed. Res. Int.* **2015**, *2015*, No. 421746.
(22) Poole, A. R.; Kojima, T.; Yasuda, T.; Mwale, F.; Kobayashi, M.; Laverty, S. Composition and structure of articular cartilage: a template for tissue repair. *Clin. Orthop. Relat. Res.* **2001**, *391*, S26−S33.
(23) Umlauf, D.; Frank, S.; Pap, T.; Bertrand, J. Cartilage biology, pathology, and repair. *Cell. Mol. Life Sci.* **2010**, *67* (24), 4197−4211.
(24) Neu, C. P.; Novak, T.; Gilliland, K. F.; Marshall, P.; Calve, S. Optical clearing in collagen- and proteoglycan-rich osteochondral tissues. *Osteoarthritis Cartilage* **2015**, *23* (3), 405−413.
(25) Martel-Pelletier, J.; Barr, A. J.; Cicuttini, F. M.; Conaghan, P. G.; Cooper, C.; Goldring, M. B.; Goldring, S. R.; Jones, G.; Teichtahl, A. J.; Pelletier, J.-P. Osteoarthritis. *Nat. Rev. Dis. Primers* **2016**, *2*, 16072.
(26) Guilak, F.; Nims, R. J.; Dicks, A.; Wu, C.-L.; Meulenbelt, I. Osteoarthritis as a disease of the cartilage pericellular matrix. *Matrix Biol.* **2018**, *71*−*72*, 40−50.
(27) Jin, X.; Deng, Z.; Wang, J.; Ye, Q.; Mei, J.; Zhou, W.; Zhang, C.; Tian, J. Study of the inhibition effect of thiazone on muscle optical clearing. *J. Biomed. Opt.* **2016**, *21* (10), No. 105004.
(28) Jing, D.; Zhang, S.; Luo, W.; Gao, X.; Men, Y.; Ma, C.; Liu, X.; Yi, Y.; Bugde, A.; Zhou, B. O.; Zhao, Z.; Yuan, Q.; Feng, J. Q.; Gao, L.; Ge, W.-P.; Zhao, H. Tissue clearing of both hard and soft tissue organs with the PEGASOS method. *Cell Res.* **2018**, *28* (8), 803−818.
(29) Chung, K.; Wallace, J.; Kim, S.-Y.; Kalyanasundaram, S.; Andalman, A. S.; Davidson, T. J.; Mirzabekov, J. J.; Zalocusky, K. A.; Mattis, J.; Denisin, A. K.; Pak, S.; Bernstein, H.; Ramakrishnan, C.; Grosenick, L.; Gradinaru, V.; Deisseroth, K. Structural and molecular interrogation of intact biological systems. *Nature* **2013**, *497* (7449), 332−337.
(30) Murray, E.; Cho, J. H.; Goodwin, D.; Ku, T.; Swaney, J.; Kim, S.-Y.; Choi, H.; Park, Y.-G.; Park, J.-Y.; Hubbert, A.; McCue, M.; Vassallo, S.; Bakh, N.; Frosch, M. P.; Wedeen, V. J.; Seung, H. S.; Chung, K. Simple, scalable proteomic imaging for high-dimensional profiling of intact systems. *Cell* **2015**, *163* (6), 1500−1514.
(31) Zhao, Y.-J.; Yu, T.-T.; Zhang, C.; Li, Z.; Luo, Q.-M.; Xu, T.-H.; Zhu, D. Skull optical clearing window for imaging of the mouse cortex at synaptic resolution. *Light Sci. Appl.* **2018**, *7*, 17153.
(32) Tainaka, K.; Murakami, T. C.; Susaki, E. A.; Shimizu, C.; Saito, R.; Takahashi, K.; Hayashi-Takagi, A.; Sekiya, H.; Arima, Y.; Nojima, S.; Ikemura, M.; Ushiku, T.; Shimizu, Y.; Murakami, M.; Tanaka, K. F.; Iino, M.; Kasai, H.; Sasaoka, T.; Kobayashi, K.; Miyazono, K.; Morii, E.; Isa, T.; Fukayama, M.; Kakita, A.; Ueda, H. R. Chemical landscape for tissue clearing based on hydrophilic reagents. *Cell Rep.* **2018**, *24* (8), 2196.
(33) Tainaka, K.; Kubota, S. I.; Suyama, T. Q.; Susaki, E. A.; Perrin, D.; Ukai-Tadenuma, M.; Ukai, H.; Ueda, H. R. Whole-body imaging with single-cell resolution by tissue decolorization. *Cell* **2014**, *159* (4), 911−924.
(34) Chung, K.; Deisseroth, K. CLARITY for mapping the nervous system. *Nat. Methods* **2013**, *10* (6), 508−513.
(35) Susaki, E. A.; Tainaka, K.; Perrin, D.; Yukinaga, H.; Kuno, A.; Ueda, H. R. Advanced CUBIC protocols for whole-brain and whole-body clearing and imaging. *Nat. Protoc* **2015**, *10* (11), 1709−1727.
(36) Ke, M.-T.; Fujimoto, S.; Imai, T. SeeDB: a simple and morphology-preserving optical clearing agent for neuronal circuit reconstruction. *Nat. Neurosci.* **2013**, *16* (8), 1154−1161.
(37) Hou, B.; Zhang, D.; Zhao, S.; Wei, M.; Yang, Z.; Wang, S.; Wang, J.; Zhang, X.; Liu, B.; Fan, L.; Li, Y.; Qiu, Z.; Zhang, C.; Jiang, T. Scalable and DiI-compatible optical clearance of the mammalian brain. *Front. Neuroanat.* **2015**, *9*, 19.
(38) Becker, K.; Jährling, N.; Saghafi, S.; Weiler, R.; Dodt, H.-U. Chemical clearing and dehydration of GFP expressing mouse brains. *PLoS One* **2012**, *7* (3), No. e33916.
(39) Schwarz, M. K.; Scherbarth, A.; Sprengel, R.; Engelhardt, J.; Theer, P.; Giese, G. Fluorescent-protein stabilization and high-resolution imaging of cleared, intact mouse brains. *PLoS One* **2015**, *10* (5), No. e0124650.
(40) Pan, C.; Cai, R.; Quacquarelli, F. P.; Ghasemigharagoz, A.; Lourbopoulos, A.; Matryba, P.; Plesnila, N.; Dichgans, M.; Hellal, F.; Ertürk, A. Shrinkage-mediated imaging of entire organs and organisms using uDISCO. *Nat. Methods* **2016**, *13* (10), 859−867.
(41) Renier, N.; Adams, E. L.; Kirst, C.; Wu, Z.; Azevedo, R.; Kohl, J.; Autry, A. E.; Kadiri, L.; Umadevi Venkataraju, K.; Zhou, Y.; Wang, V. X.; Tang, C. Y.; Olsen, O.; Dulac, C.; Osten, P.; Tessier-Lavigne, M. Mapping of brain activity by automated volume analysis of immediate early genes. *Cell* **2016**, *165* (7), 1789−1802.
(42) Ertürk, A.; Mauch, C. P.; Hellal, F.; Förstner, F.; Keck, T.; Becker, K.; Jährling, N.; Steffens, H.; Richter, M.; Hübener, M.; Kramer, E.; Kirchhoff, F.; Dodt, H. U.; Bradke, F. Three-dimensional imaging of the unsectioned adult spinal cord to assess axon regeneration and glial responses after injury. *Nat. Med.* **2012**, *18* (1), 166−171.
(43) Hama, H.; Kurokawa, H.; Kawano, H.; Ando, R.; Shimogori, T.; Noda, H.; Fukami, K.; Sakaue-Sawano, A.; Miyawaki, A. Scale: a chemical approach for fluorescence imaging and reconstruction of transparent mouse brain. *Nat. Neurosci.* **2011**, *14* (11), 1481−1488.
(44) Park, Y.-G.; Sohn, C. H.; Chen, R.; McCue, M.; Yun, D. H.; Drummond, G. T.; Ku, T.; Evans, N. B.; Oak, H. C.; Trieu, W.; Choi, H.; Jin, X.; Lilascharoen, V.; Wang, J.; Truttmann, M. C.; Qi, H. W.; Ploegh, H. L.; Golub, T. R.; Chen, S.-C.; Frosch, M. P.; Kulik, H. J.; Lim, B. K.; Chung, K. Protection of tissue physicochemical properties using polyfunctional crosslinkers. *Nat. Biotechnol.* **2019**, *37*, 73.
(45) Yang, B.; Treweek, J. B.; Kulkarni, R. P.; Deverman, B. E.; Chen, C.-K.; Lubeck, E.; Shah, S.; Cai, L.; Gradinaru, V. Single-cell phenotyping within transparent intact tissue through whole-body clearing. *Cell* **2014**, *158* (4), 945−958.
(46) Feng, Y.; Yu, Z. W.; Quinn, P. J. Effect of urea, dimethylurea, and tetramethylurea on the phase behavior of dioleoylphosphatidylethanolamine. *Chem. Phys. Lipids* **2002**, *114* (2), 149−157.
(47) Ke, M.-T.; Nakai, Y.; Fujimoto, S.; Takayama, R.; Yoshida, S.; Kitajima, T. S.; Sato, M.; Imai, T. Super-resolution mapping of neuronal circuitry with an index-optimized clearing agent. *Cell Rep.* **2016**, *14* (11), 2718−2732.

https://doi.org/10.1021/acsomega.2c05180
ACS Omega 2023, 8, 1739−1758

(48) Susaki, E. A.; Ueda, H. R. Whole-body and whole-organ clearing and imaging techniques with single-cell resolution: toward organism-level systems biology in mammals. *Cell Chem. Biol.* **2016**, *23* (1), 137−157.
(49) Susaki, E. A.; Tainaka, K.; Perrin, D.; Kishino, F.; Tawara, T.; Watanabe, T. M.; Yokoyama, C.; Onoe, H.; Eguchi, M.; Yamaguchi, S.; Abe, T.; Kiyonari, H.; Shimizu, Y.; Miyawaki, A.; Yokota, H.; Ueda, H. R. Whole-brain imaging with single-cell resolution using chemical cocktails and computational analysis. *Cell* **2014**, *157* (3), 726−739.
(50) Richardson, D. S.; Lichtman, J. W. Clarifying tissue clearing. *Cell* **2015**, *162* (2), 246−257.
(51) Liang, X.; Luo, H. Optical tissue clearing: illuminating brain function and dysfunction. *Theranostics* **2021**, *11* (7), 3035−3051.
(52) Dodt, H.-U.; Leischner, U.; Schierloh, A.; Jährling, N.; Mauch, C. P.; Deininger, K.; Deussing, J. M.; Eder, M.; Zieglgänsberger, W.; Becker, K. Ultramicroscopy: three-dimensional visualization of neuronal networks in the whole mouse brain. *Nat. Methods* **2007**, *4* (4), 331−336.
(53) Renier, N.; Wu, Z.; Simon, D. J.; Yang, J.; Ariel, P.; Tessier-Lavigne, M. iDISCO: a simple, rapid method to immunolabel large tissue samples for volume imaging. *Cell* **2014**, *159* (4), 896−910.
(54) Klingberg, A.; Hasenberg, A.; Ludwig-Portugall, I.; Medyukhina, A.; Männ, L.; Brenzel, A.; Engel, D. R.; Figge, M. T.; Kurts, C.; Gunzer, M. Fully automated evaluation of total glomerular number and capillary tuft size in nephritic kidneys using lightsheet microscopy. *J. Am. Soc. Nephrol.* **2017**, *28* (2), 452−459.
(55) Perbellini, F.; Liu, A. K. L.; Watson, S. A.; Bardi, I.; Rothery, S. M.; Terracciano, C. M. Free-of-Acrylamide SDS-based Tissue Clearing (FASTClear) for three dimensional visualization of myocardial tissue. *Sci. Rep.* **2017**, *7* (1), 5188.
(56) Cai, R.; Pan, C.; Ghasemigharagoz, A.; Todorov, M. I.; Förstera, B.; Zhao, S.; Bhatia, H. S.; Parra-Damas, A.; Mrowka, L.; Theodorou, D.; Rempfler, M.; Xavier, A. L. R.; Kress, B. T.; Benakis, C.; Steinke, H.; Liebscher, S.; Bechmann, I.; Liesz, A.; Menze, B.; Kerschensteiner, M.; Nedergaard, M.; Ertürk, A. Panoptic imaging of transparent mice reveals whole-body neuronal projections and skull-meninges connections. *Nat. Neurosci.* **2019**, *22* (2), 317−327.
(57) Qi, Y.; Yu, T.; Xu, J.; Wan, P.; Ma, Y.; Zhu, J.; Li, Y.; Gong, H.; Luo, Q.; Zhu, D. FDISCO: Advanced solvent-based clearing method for imaging whole organs. *Sci. Adv.* **2019**, *5* (1), No. eaau8355.
(58) Hahn, C.; Becker, K.; Saghafi, S.; Pende, M.; Avdibašić, A.; Foroughipour, M.; Heinz, D. E.; Wotjak, C. T.; Dodt, H.-U. High-resolution imaging of fluorescent whole mouse brains using stabilised organic media (sDISCO). *J. Biophotonics* **2019**, *12* (8), No. e201800368.
(59) Zhan, Y.; Wu, H.; Liu, L.; Lin, J.; Zhang, S. Organic solvent-based tissue clearing techniques and their applications. *J. Biophotonics* **2021**, *14* (6), No. e202000413.
(60) Tsai, P. S.; Kaufhold, J. P.; Blinder, P.; Friedman, B.; Drew, P. J.; Karten, H. J.; Lyden, P. D.; Kleinfeld, D. Correlations of neuronal and microvascular densities in murine cortex revealed by direct counting and colocalization of nuclei and vessels. *J. Neurosci.* **2009**, *29* (46), 14553−14570.
(61) Song, E.; Seo, H.; Choe, K.; Hwang, Y.; Ahn, J.; Ahn, S.; Kim, P. Optical clearing based cellular-level 3D visualization of intact lymph node cortex. *Biomed. Opt. Express* **2015**, *6* (10), 4154−4164.
(62) Kuwajima, T.; Sitko, A. A.; Bhansali, P.; Jurgens, C.; Guido, W.; Mason, C. ClearT: a detergent- and solvent-free clearing method for neuronal and non-neuronal tissue. *Development* **2013**, *140* (6), 1364−8.
(63) Zhu, J.; Yu, T.; Li, Y.; Xu, J.; Qi, Y.; Yao, Y.; Ma, Y.; Wan, P.; Chen, Z.; Li, X.; Gong, H.; Luo, Q.; Zhu, D. MACS: Rapid Aqueous Clearing System for 3D Mapping of Intact Organs. *Adv. Sci. (Weinheim, Baden-Wurttemberg, Germany)* **2020**, *7* (8), No. 1903185.
(64) Hama, H.; Hioki, H.; Namiki, K.; Hoshida, T.; Kurokawa, H.; Ishidate, F.; Kaneko, T.; Akagi, T.; Saito, T.; Saido, T.; Miyawaki, A. ScaleS: an optical clearing palette for biological imaging. *Nat. Neurosci.* **2015**, *18* (10), 1518−1529.
(65) Ke, M. T.; Nakai, Y.; Fujimoto, S.; Takayama, R.; Yoshida, S.; Kitajima, T. S.; Sato, M.; Imai, T. Super-Resolution Mapping of Neuronal Circuitry With an Index-Optimized Clearing Agent. *Cell Rep.* **2016**, *14* (11), 2718−32.
(66) Treweek, J. B.; Chan, K. Y.; Flytzanis, N. C.; Yang, B.; Deverman, B. E.; Greenbaum, A.; Lignell, A.; Xiao, C.; Cai, L.; Ladinsky, M. S.; Bjorkman, P. J.; Fowlkes, C. C.; Gradinaru, V. Whole-body tissue stabilization and selective extractions via tissue-hydrogel hybrids for high-resolution intact circuit mapping and phenotyping. *Nat. Protoc.* **2015**, *10* (11), 1860−1896.
(67) Sung, K.; Ding, Y.; Ma, J.; Chen, H.; Huang, V.; Cheng, M.; Yang, C. F.; Kim, J. T.; Eguchi, D.; Di Carlo, D.; Hsiai, T. K.; Nakano, A.; Kulkarni, R. P. Simplified three-dimensional tissue clearing and incorporation of colorimetric phenotyping. *Sci. Rep.* **2016**, *6*, No. 30736.
(68) Weiss, K. R.; Voigt, F. F.; Shepherd, D. P.; Huisken, J. Tutorial: practical considerations for tissue clearing and imaging. *Nat. Protoc.* **2021**, *16* (6), 2732−2748.
(69) Dickie, R.; Bachoo, R. M.; Rupnick, M. A.; Dallabrida, S. M.; Deloid, G. M.; Lai, J.; Depinho, R. A.; Rogers, R. A. Three-dimensional visualization of microvessel architecture of whole-mount tissue by confocal microscopy. *Microvasc. Res.* **2006**, *72* (1−2), 20−26.
(70) Milgroom, A.; Ralston, E. Clearing skeletal muscle with CLARITY for light microscopy imaging. *Cell Biol. Int.* **2016**, *40* (4), 478−483.
(71) Zhang, W. L.; Liu, S. H.; Zhang, W. C.; Hu, W.; Jiang, M.; Tamadon, A.; Feng, Y. Skeletal muscle CLARITY: a preliminary study of imaging the three-dimensional architecture of blood vessels and neurons. *Cell J.* **2018**, *20* (2), 132−137.
(72) Williams, M. P. I.; Rigon, M.; Straka, T.; Hörner, S. J.; Thiel, M.; Gretz, N.; Hafner, M.; Reischl, M.; Rudolf, R. A novel optical tissue clearing protocol for mouse skeletal muscle to visualize endplates in their tissue context. *Front. Cell Neurosci.* **2019**, *13*, 49.
(73) Yin, X.; Yu, T.; Chen, B.; Xu, J.; Chen, W.; Qi, Y.; Zhang, P.; Li, Y.; Kou, Y.; Ma, Y.; Han, N.; Wan, P.; Luo, Q.; Zhu, D.; Jiang, B. Spatial distribution of motor endplates and its adaptive change in skeletal muscle. *Theranostics* **2019**, *9* (3), 734−746.
(74) Chen, W.; Yu, T.; Chen, B.; Qi, Y.; Zhang, P.; Zhu, D.; Yin, X.; Jiang, B. In vivo injection of α-bungarotoxin to improve the efficiency of motor endplate labeling. *Brain Behav.* **2016**, *6* (6), No. e00468.
(75) Xu, J.; Xuan, A.; Liu, Z.; Li, Y.; Zhu, J.; Yao, Y.; Yu, T.; Zhu, D. An approach to maximize retrograde transport based on the spatial distribution of motor endplates in mouse hindlimb muscles. *Front. Cell Neurosci.* **2021**, *15*, No. 707982.
(76) Li, D.-D.; Deng, J.; Jin, B.; Han, S.; Gu, X.-Y.; Zhou, X.-F.; Yin, X.-F. Effects of delayed repair of peripheral nerve injury on the spatial distribution of motor endplates in target muscle. *Neural Regener. Res.* **2022**, *17* (2), 459−464.
(77) Schneidereit, D.; Bröllochs, A.; Ritter, P.; Kreiß, L.; Mokhtari, Z.; Beilhack, A.; Krönke, G.; Ackermann, J. A.; Faas, M.; Grüneboom, A.; Schürmann, S.; Friedrich, O. An advanced optical clearing protocol allows label-free detection of tissue necrosis multiphoton microscopy in injured whole muscle. *Theranostics* **2021**, *11* (6), 2876−2891.
(78) Bozycki, L.; Łukasiewicz, K.; Matryba, P.; Pikula, S. Whole-body clearing, staining and screening of calcium deposits in the mdx mouse model of Duchenne muscular dystrophy. *Skeletal Muscle* **2018**, *8* (1), 21.
(79) Decroix, L.; Van Muylder, V.; Desender, L.; Sampaolesi, M.; Thorrez, L. Tissue clearing for confocal imaging of native and bio-artificial skeletal muscle. *Biotech. Histochem.* **2015**, *90* (6), 424−431.
(80) Ariyasinghe, N. R.; Santoso, J. W.; Gupta, D.; Pincus, M. J.; August, P. R.; McCain, M. L. Optical clearing of skeletal muscle bundles engineered in 3-d printed templates. *Ann. Biomed. Eng.* **2021**, *49* (2), 523−535.
(81) Fei, P.; Lee, J.; Packard, R. R. S.; Sereti, K.-I.; Xu, H.; Ma, J.; Ding, Y.; Kang, H.; Chen, H.; Sung, K.; Kulkarni, R.; Ardehali, R.; Kuo, C. C. J.; Xu, X.; Ho, C.-M.; Hsiai, T. K. Cardiac light-sheet

https://doi.org/10.1021/acsomega.2c05180
ACS Omega 2023, 8, 1739−1758

fluorescent microscopy for multi-scale and rapid imaging of architecture and function. *Sci. Rep.* **2016**, *6*, No. 22489.
(82) Ding, Y.; Lee, J.; Ma, J.; Sung, K.; Yokota, T.; Singh, N.; Dooraghi, M.; Abiri, P.; Wang, Y.; Kulkarni, R. P.; Nakano, A.; Nguyen, T. P.; Fei, P.; Hsiai, T. K. Light-sheet fluorescence imaging to localize cardiac lineage and protein distribution. *Sci. Rep.* **2017**, *7*, No. 42209.
(83) Watson, S. A.; Terracciano, C. M.; Perbellini, F. Myocardial slices: an intermediate complexity platform for translational cardiovascular research. *Cardiovasc. Drugs Ther.* **2019**, *33* (2), 239−244.
(84) Sommer, G.; Schriefl, A. J.; Andrä, M.; Sacherer, M.; Viertler, C.; Wolinski, H.; Holzapfel, G. A. Biomechanical properties and microstructure of human ventricular myocardium. *Acta Biomater.* **2015**, *24*, 172−192.
(85) Yu, J.; Seldin, M. M.; Fu, K.; Li, S.; Lam, L.; Wang, P.; Wang, Y.; Huang, D.; Nguyen, T. L.; Wei, B.; Kulkarni, R. P.; Di Carlo, D.; Teitell, M.; Pellegrini, M.; Lusis, A. J.; Deb, A. Topological arrangement of cardiac fibroblasts regulates cellular plasticity. *Circ. Res.* **2018**, *123* (1), 73−85.
(86) Fischesser, D. M.; Meyer, E. C.; Sargent, M.; Molkentin, J. D. Refined CLARITY-based tissue clearing for three-dimensional fibroblast organization in healthy and injured mouse hearts. *J. Vis. Exp.* **2021**, No. 171, e62023.
(87) Lee, S.-E.; Nguyen, C.; Yoon, J.; Chang, H.-J.; Kim, S.; Kim, C. H.; Li, D. Three-dimensional cardiomyocytes structure revealed by diffusion tensor imaging and its validation using a tissue-clearing technique. *Sci. Rep.* **2018**, *8* (1), 6640.
(88) Kagami, K.; Ono, M.; Iizuka, T.; Matsumoto, T.; Hosono, T.; Sekizuka-Kagami, N.; Shinmyo, Y.; Kawasaki, H.; Fujiwara, H. A novel third mesh-like myometrial layer connects the longitudinal and circular muscle fibers-A potential stratum to coordinate uterine contractions. *Sci. Rep.* **2020**, *10* (1), 8274.
(89) Yang, X.; Zhang, Y.; Zhao, K.; Zhao, Y.; Liu, Y.; Gong, H.; Luo, Q.; Zhu, D. Skull optical clearing solution for enhancing ultrasonic and photoacoustic imaging. *IEEE Trans. Med. Imaging* **2016**, *35* (8), 1903−1906.
(90) Wang, J.; Zhang, Y.; Xu, T. H.; Luo, Q. M.; Zhu, D. An innovative transparent cranial window based on skull optical clearing. *Laser Phys. Lett.* **2012**, *9* (6), 469.
(91) Zhang, C.; Feng, W.; Zhao, Y.; Yu, T.; Li, P.; Xu, T.; Luo, Q.; Zhu, D. A large, switchable optical clearing skull window for cerebrovascular imaging. *Theranostics* **2018**, *8* (10), 2696−2708.
(92) Chen, Y.; Liu, S.; Liu, H.; Tong, S.; Tang, H.; Zhang, C.; Yan, S.; Li, H.; Yang, G.; Zhu, D.; Wang, K.; Wang, P. Coherent raman scattering unravelling mechanisms underlying skull optical clearing for through-skull brain imaging. *Anal. Chem.* **2019**, *91* (15), 9371−9375.
(93) Li, D.-Y.; Zheng, Z.; Yu, T.-T.; Tang, B.-Z.; Fei, P.; Qian, J.; Zhu, D. Visible-near infrared-II skull optical clearing window for in vivo cortical vasculature imaging and targeted manipulation. *J. Biophotonics* **2020**, *13* (10), No. e202000142.
(94) Vandeweghe, S.; Coelho, P. G.; Vanhove, C.; Wennerberg, A.; Jimbo, R. Utilizing micro-computed tomography to evaluate bone structure surrounding dental implants: a comparison with histomorphometry. *J. Biomed. Mater. Res., Part B* **2013**, *101* (7), 1259−1266.
(95) Yi, Y.; Men, Y.; Jing, D.; Luo, W.; Zhang, S.; Feng, J. Q.; Liu, J.; Ge, W.-P.; Wang, J.; Zhao, H. 3-dimensional visualization of implant-tissue interface with the polyethylene glycol associated solvent system tissue clearing method. *Cell Prolif.* **2019**, *52* (3), No. e12578.
(96) Yi, Y.; Stenberg, W.; Luo, W.; Feng, J. Q.; Zhao, H. Alveolar bone marrow Gli1+ stem cells support implant osseointegration. *J. Dent. Res.* **2022**, *101* (1), 73−82.
(97) Zhang, D.; Zhang, S.; Wang, J.; Li, Q.; Xue, H.; Sheng, R.; Xiong, Q.; Qi, X.; Wen, J.; Fan, Y.; Zhou, B. O.; Yuan, Q. LepR-expressing stem cells are essential for alveolar bone regeneration. *J. Dent. Res.* **2020**, *99* (11), 1279−1286.
(98) Grüneboom, A.; Hawwari, I.; Weidner, D.; Culemann, S.; Müller, S.; Henneberg, S.; Brenzel, A.; Merz, S.; Bornemann, L.; Zec, K.; Wuelling, M.; Kling, L.; Hasenberg, M.; Voortmann, S.; Lang, S.; Baum, W.; Ohs, A.; Kraff, O.; Quick, H. H.; Jäger, M.; Landgraeber, S.; Dudda, M.; Danuser, R.; Stein, J. V.; Rohde, M.; Gelse, K.; Garbe, A. I.; Adamczyk, A.; Westendorf, A. M.; Hoffmann, D.; Christiansen, S.; Engel, D. R.; Vortkamp, A.; Krönke, G.; Herrmann, M.; Kamradt, T.; Schett, G.; Hasenberg, A.; Gunzer, M. A network of trans-cortical capillaries as mainstay for blood circulation in long bones. *Nat. Metab.* **2019**, *1* (2), 236−250.
(99) Luo, W.; Yi, Y.; Jing, D.; Zhang, S.; Men, Y.; Ge, W.-P.; Zhao, H. Investigation of postnatal craniofacial bone development with tissue clearing-based three-dimensional imaging. *Stem Cells Dev.* **2019**, *28* (19), 1310−1321.
(100) Gorelashvili, M. G.; Heinze, K. G.; Stegner, D. Optical clearing of murine bones to study megakaryocytes in intact bone marrow using light-sheet fluorescence microscopy. *Methods Mol. Biol.* **2018**, *1812*, 233−253.
(101) Greenbaum, A.; Chan, K. Y.; Dobreva, T.; Brown, D.; Balani, D. H.; Boyce, R.; Kronenberg, H. M.; McBride, H. J.; Gradinaru, V. Bone CLARITY: Clearing, imaging, and computational analysis of osteoprogenitors within intact bone marrow. *Sci. Transl. Med.* **2017**, *9* (387), eaah6518.
(102) Masselink, W.; Reumann, D.; Murawala, P.; Pasierbek, P.; Taniguchi, Y.; Bonnay, F.; Meixner, K.; Knoblich, J. A.; Tanaka, E. M. Broad applicability of a streamlined ethyl cinnamate-based clearing procedure. *Development* **2019**, *146* (3), dev166884.
(103) Calve, S.; Ready, A.; Huppenbauer, C.; Main, R.; Neu, C. P. Optical clearing in dense connective tissues to visualize cellular connectivity in situ. *PLoS One* **2015**, *10* (1), No. e0116662.
(104) Arnoczky, S. P.; Warren, R. F. Microvasculature of the human meniscus. *Am. J. Sports Med.* **1982**, *10* (2), 90−95.
(105) Arnoczky, S. P.; Warren, R. F. The microvasculature of the meniscus and its response to injury: An experimental study in the dog. *Am. J. Sports Med.* **1983**, *11* (3), 131−141.
(106) Bednar, M. S.; Arnoczky, S. P.; Weiland, A. J. The microvasculature of the triangular fibrocartilage complex: its clinical significance. *J. Hand Surg. Am.* **1991**, *16* (6), 1101−1105.
(107) Crawford, M. D.; Hellwinkel, J. E.; Aman, Z.; Akamefula, R.; Singleton, J. T.; Bahney, C.; LaPrade, R. F. Microvascular anatomy and intrinsic gene expression of menisci from young adults. *Am. J. Sports Med.* **2020**, *48* (13), 3147−3153.
(108) Crock, H. V.; Crock, M. C. The Blood Supply of the Lower Limb Bones in Man (Descriptive and Applied). *J. Anat.* **1967**, *102*, 131.
(109) Bykov, A.; Hautala, T.; Kinnunen, M.; Popov, A.; Karhula, S.; Saarakkala, S.; Nieminen, M. T.; Tuchin, V.; Meglinski, I. Imaging of subchondral bone by optical coherence tomography upon optical clearing of articular cartilage. *J. Biophotonics* **2016**, *9* (3), 270−275.
(110) Bykov, A.; Hautala, T.; Kinnunen, M.; Popov, A.; Karhula, S.; Saarakkala, S.; Nieminen, M. T.; Tuchin, V., Optical clearing of articular cartilage: A comparison of clearing agents. In *Novel Biophotonics Techniques and Applications III*; Amelink, A, Vitkin, I. A., Eds.; SPIE Proceedings, Vol. *9540*; Optica, 2015; 95400A. DOI: 10.1364/ECBO.2015.95400A.
(111) Alexandrovskaya, Y.; Sadovnikov, K.; Sharov, A.; Sherstneva, A.; Evtushenko, E.; Omelchenko, A.; Obrezkova, M.; Tuchin, V.; Lunin, V.; Sobol, E. Controlling the near-infrared transparency of costal cartilage by impregnation with clearing agents and magnetite nanoparticles. *J. Biophotonics* **2018**, *11* (2), e201700105.
(112) Alexandrovskaya, Y. M.; Evtushenko, E. G.; Obrezkova, M. M.; Tuchin, V. V.; Sobol, E. N. Control of optical transparency and infrared laser heating of costal cartilage via injection of iohexol. *J. Biophotonics* **2018**, *11* (12), No. e201800195.
(113) Bales, C. P.; Placzek, J. D.; Malone, K. J.; Vaupel, Z.; Arnoczky, S. P. Microvascular supply of the lateral epicondyle and common extensor origin. *J. Shoulder Elbow Surg.* **2007**, *16* (4), 497−501.
(114) Brown, E.; McKee, T.; diTomaso, E.; Pluen, A.; Seed, B.; Boucher, Y.; Jain, R. K. Dynamic imaging of collagen and its

modulation in tumors in vivo using second-harmonic generation. *Nat. Med.* **2003**, *9* (6), 796−800.
(115) Huisken, J.; Swoger, J.; Del Bene, F.; Wittbrodt, J.; Stelzer, E. H. K. Optical sectioning deep inside live embryos by selective plane illumination microscopy. *Science* **2004**, *305* (5686), 1007−1009.
(116) Verma, M.; Murkonda, B., Sr.; Asakura, Y.; Asakura, A. Skeletal muscle tissue clearing for LacZ and fluorescent reporters, and immunofluorescence staining. *Methods Mol. Biol.* **2016**, *1460*, 129−140.

https://doi.org/10.1021/acsomega.2c05180
ACS Omega 2023, 8, 1739−1758